Potential link between structure of iron catalyst and Fenton-like performance: from fundamental understanding to engineering design

Ling Li [a, 1], Zhuo Yin [b, 1], Min Cheng [a], Lei Qin [a], Shiyu Liu [a], Huan Yi [a], Mingming Zhang [a], Yukui Fu [a], Lu Yang [a], Chensi Tang [a], Xuerong Zhou [a], Fuhang Xu [a], Guangming Zeng [a, *], Cui Lai [a, *]

[a] *College of Environmental Science and Engineering and Key Laboratory of Environmental Biology and Pollution Control (Ministry of Education), Hunan University, Changsha, 410082, P R China*

[b] *Department of Urology, Second Xiangya Hospital, Central South University, Changsha 410011, P R China*

---

* Corresponding author.

E-mail address: zgming@hnu.edu.cn (G.M. Zeng) and laicui@hnu.edu.cn (C.Lai).

[1] These authors contribute equally to this article.

Abstract

Heterogeneous Fenton-like process on the basis of Fe catalysts has been widely studied for wastewater treatment, which overcomes the problem of pH limitation and sludge production in homogeneous Fenton system. Nevertheless, excessive H_2O_2 is typically required to reach a desirable Fenton-like efficiency of Fe catalysts, challenging the environmentally sustainable application. Hence, numerous researches have been carried out to improve the utilization efficiency of Fe catalysts to H_2O_2. Among various strategies, structure design is possible to endow Fe catalysts with novel physiochemical properties, such as different coordination environment, more active sites and enhanced charge transfer, which has attracted wide interest with tremendous research progress being made. In this review, we mainly focus on the recent advances in designing "smart" Fe catalysts for efficient Fenton-like reaction through structure design. The influence mechanisms of some structure properties (i.e., exposed facet, defects, catalyst size, and space confinement) on the Fenton-like activity of Fe catalysts are carefully discussed to generalize structure-activity relationships. Afterward, we will briefly summarize the characterization techniques for examining these structure properties, followed by strategies to prepare Fe catalysts with specific structure. This review intends to offer valuable information for designing and fabricating efficient environmental catalysts for the heterogeneous Fenton-like reaction.

Keywords: Heterogeneous Fenton-like process; Fe catalysts; Structure-activity relationships; Characterization; Structural design

1 Introduction

With the inevitable industrialization and urbanization, the environmental pollution has developed into a global challenge damaging the ecosystem and plaguing the survival of life.[1-3] Therefore, environmental remediation has received much attention, finding environmental-friendly techniques to remove contaminants from various media is of highly urgent.[4-6] Recently, advanced oxidation processes (AOPs) have been regarded as attractive technologies to destruct toxic and recalcitrant pollutants, on account of the generation of highly reactive species.[7-10] Fenton process is one of the most representative AOPs, which consists of the production of hydroxyl radical (•OH) via the interaction between Fe^{2+} and hydrogen peroxide (H_2O_2) (Eq. 1).[11, 12] Regrettably, in spite of its powerful oxidation capacity, homogeneous Fenton process keeps facing several limitations, such as narrow working pH (pH 2.8-3.5), accumulation of Fe-containing sludge, and difficulty in catalyst recycling.[13] To this end, researchers have deflected to develop heterogeneous Fenton-like processes based on solid catalysts. The development of efficacious heterogeneous catalyst is significant to the application of this technology.

Currently, multivalent transition metal (i.e., Fe, Mn, Cu and Co) based catalysts have been extensively employed as H_2O_2 activator, because of their capacity of participating in the electron transfer reaction with H_2O_2 and possible auxiliary functions (such as magnetic separation).[14-16] In particular, Fe catalysts show great potential as heterogeneous Fenton-like catalysts since Fe is the second most abundant metal in nature and almost non-toxic, besides, the important role of Fe in classical homogeneous

Fenton process has been widely studied.[17, 18] To date, multifarious Fe catalysts have been successively applied in heterogeneous Fenton-like reaction, such as zero-valent Fe,[19, 20] Fe oxides,[21, 22] Fe-based sulfide,[23, 24] Fe-based layered double hydroxides (LDHs),[25, 26] and Fe-based metal-organic frameworks (MOFs),[21, 27] which do exhibit good Fenton-like catalytic activity. Nevertheless, a large excess of H_2O_2 (above the stoichiometric amount by 100-fold) are typically required to achieve a desirable Fenton-like performance of Fe catalysts,[28] due to the necessary cycle of Fe^{2+} and Fe^{3+} for •OH generation (Eq. 1), and the regeneration of Fe^{2+} via reduction of Fe^{3+} (rate-limiting step) (Eq. 2),[29] resulting in the limitation of practical application.

$$Fe^{2+} + H_2O_2 \rightarrow Fe^{3+} + HO^{-} + \cdot OH \qquad k = 40\text{-}80\ M^{-1}s^{-1} \tag{1}$$

$$Fe^{3+} + H_2O_2 \rightarrow Fe^{2+} + H^{+} + HO_2\cdot \qquad k = 0.001\text{-}0.01\ M^{-1}s^{-1} \tag{2}$$

It is thus required to improve the utilization efficiency of Fe catalysts to H_2O_2 to reduce the consumption of H_2O_2. In general, heterogeneous Fenton-like processes are highly dependent on surface reactions to activate H_2O_2 to generate reactive species.[22, 30] Therefore, it can be considered that surface structure of Fe catalysts (i.e., atom arrangement, coordination environment, and electronic structure, etc.) have a significant impact on their Fenton-like activity.[12, 31, 32] For example, it is well-known that H_2O_2 (Lewis base) tend to adsorb on unsaturated coordinated Fe atoms (Lewis acid sites) on catalysts surface with strong affinity,[33, 34] and coordination number of active sites usually have a significant effect on the adsorption process. To be specific, the active sites possessing low atomic coordination number generally exhibit strong adsorption ability, while too higher undercoordination number of active sites might disfavor the adsorption process owing to the relatively strong stereo-hindrance effect.[31, 35, 36] In this regard, the different coordination environment of Fe, which closely relate to the particle size and exposed surface,[35, 37, 38] will correspondingly affect H_2O_2 complexation and adsorption, and thus H_2O_2 activation. Meanwhile, the charge transfer from catalysts to H_2O_2 also plays a significant role in activating H_2O_2, and sufficient charge transfer would effectively promote catalytic activity of catalysts. Accordingly, many strategies to optimize the electronic structure of Fe catalysts have been proposed, such as introducing oxygen vacancies, which can not only facilitate surface Fe^{3+}/Fe^{2+} redox cycle, but also promote charge transfer from catalysts to adsorbed H_2O_2, thereby improving H_2O_2 utilization efficiency and Fenton-like catalytic performance.[39-41] As a whole, structure design of Fe catalysts to modulate surface structure brings about new opportunities for improving Fenton-like catalytic activity. A systematic understanding of the relationship between Fenton-like catalytic activity/mechanisms and structural characteristics is thus in urgent need for future construction of highly efficient Fe catalysts.

Currently, a number of reviews have summarized the types of Fe catalysts in heterogeneous Fenton-like process and strategies to improve catalytic performance through additional energy input, such as light, ultrasound, and chelating agents.[12, 17, 31, 42-44] These reviews made great progress in summarizing and promoting the application of heterogeneous Fenton-like process based on Fe catalysts. However, to the best of our knowledge, there is no review focus on the structure design of Fe catalysts towards enhanced Fenton-like process. In this critical review, we begin with the specific influence of structural properties of Fe catalysts including exposed surface, defects, catalyst size, and space confinement on Fenton-like activity, which have typical impacts on the atomic and electronic structure of catalysts, and then, the advanced characterization techniques for evaluating the structure-performance relationship are introduced. Besides, the structure engineering strategies are also discussed in detail. It is hoped that the available and up-to-date information in this review will inspire researchers to further design heterogeneous catalysts from the respects of structure design to maximize their potential for environmental remediation.

2 Key features of structure

In order to make a full advantage of structure design of Fe catalysts for Fenton-like catalysis, it is necessary to better understand the influence mechanism of structure properties on the Fenton-like catalytic performance. In this section, we emphasize some key features of structure, including exposed surface, defects, catalyst size, and space confinement, which significantly affect the surface structures of Fe catalysts, and thus Fenton-like performances.

2.1 Exposed surface

To date, numerous studies have demonstrated that rationally modulating exposed surface of Fe catalysts is an available strategy to enhance their Fenton-like catalytic activity, because the distinguishing surface atomic configuration and coordination on different surface usually have a notable impact on the surface reactivity.[35, 45-47] Here, the substantial role of Fe catalysts surface in affecting Fenton-like reaction will be demonstrated from the perspective of H_2O_2 adsorption, surface electronic structures relating to H_2O_2 activation, and •OH transformation.

Generally, the effective adsorption of H_2O_2 on Fe catalysts surface is considered as the prerequisite for subsequent H_2O_2 activation process. In a typical process, H_2O_2 can be molecularly adsorbed onto catalysts via the interaction between hydroxyl groups of H_2O_2 and those on the catalysts surface, the interaction between O atoms of H_2O_2 and surface exposed metal atoms, or other surface process.[48, 49] The adsorption behaviors are closely related to the atomic arrangement over catalysts surface. Therefore, it can be inferred that the exposed surface with different atomic arrangement is possible to influence the chemisorption state of H_2O_2 on surface, and then affecting the catalytic process.[50-52] For example, Dai et al. reported that $CuFeO_2$ (110) surface exposed more Fe and Cu atoms than $CuFeO_2$ (012) surface, while the exposure of O, Fe, and Cu atoms were more uniformly on (012) surface. Consequently, the chemisorption state of H_2O_2 on these two surfaces were different, and the favorable configuration between H_2O_2 and (012) surface was formed with O-H-O bond (1.749 Å) smaller than that on (110) surface (2.472 Å), and O-O bond within H_2O_2 being suitably elongated (from 1.468 Å to 1.472 Å), which favored electron transfer and •OH generation (Fig. 1(A-D)).[53] Likewise, H_2O_2 could be adsorbed onto Fe-Co Prussian blue analogues (100) and (111) surface with different chemisorption state and adsorption energy, which subsequently had an effect on the generation of •OH.[52]

In addition, according to previous researches, the different atomic arrangements and coordination in each surface will also lead to anisotropic surface electronic structures and thus surface charge states,[38, 54, 55] which may correspondingly result in the variation of charge transfer from catalysts to H_2O_2. As revealed by Chan et al., there were three types of OH groups including singly coordinated OH groups ($OH_{(I)}$), doubly coordinated OH groups ($OH_{(II)}$), and triply coordinated OH groups ($OH_{(III)}$) on hematite surface. As seen from Fig. 1(E-H), Fe atoms would coordinate with different types and numbers of OH groups at each exposed surface. Consequently, Fe atoms on α-Fe_2O_3 (001), (104), and (113) surfaces exhibited different oxidation states due to the distinguishing coordination environment. To be specific, Fe cations on (001) surface was mainly existed in valence state of 3+, and primarily showed an oxidation state between 2+ and 3+ on (113) and (104) surfaces. The hematite (113) and (104) surfaces were thus more easily to initiate an electron transfer to activate H_2O_2.[38] Besides, Huang et al. draw a conclusion that surface-reactivity differences appeared to be more relevant with the extent of undercoordination of Fe site rather than their simple aerial density. They found that hematite (012) surface possessed higher densities of undercoordinated Fe sites (singly undercoordinated Fe action activate sites (Fe_{1uc})) than hematite (001) surface (3-fold undercoordinated Fe action activate sites (Fe_{3uc})), while hematite (001) surface showed higher photo-Fenton catalytic activity. This might be because more highly undercoordinated surface Fe^{3+} were more readily reduced to Fe^{2+}, then promoting H_2O_2 activation and •OH generation.[30]

Furthermore, when H_2O_2 is dissociated to •OH at catalysts surface, the generated •OH may either bound to the surface (•$OH_{surface}$) or diffused to the solution (•OH_{free}).[56-58] This is thought to be related to the catalysts surface structure because the different atoms arrangement may affect the binding of •OH to catalysts surface. For instance, Li et al. revealed that high-density oxygen atoms on BiOCl (001) surface tended to impede the binding of •OH to surface owing to their steric hindrance, while the $\mathrm{Bi_{3c}}$ sites on BiOCl (010) surface could provide Lewis-acid sites for stabilization of •OH. Therefore, •$\mathrm{OH_{free}}$ was primarily generated when employing BiOCl (001) as Fenton-like catalyst, and •$\mathrm{OH_{surface}}$ was dominant in BiOCl (010)/H_2O_2 system.[57] By this way, the non-selectively •OH is possible to selectively degrade organic pollutants during Fenton-like reaction since •$\mathrm{OH_{surface}}$ prefer to react with organic pollutants showing high affinity to catalysts surface, and organic pollutants with low affinity to catalysts surface could be easily oxidized by •$\mathrm{OH_{free}}$. However, the relevant studies in Fe catalysts-based Fenton-like reaction are rare, which needs more research focus in the future.

Overall, the exposed surface of Fe catalysts is an important factor to affect Fenton-like performance owing to the close ties between surface properties and H_2O_2 activation. Nevertheless, it should be noted that single crystal facets of metallic Fe do not have any application potentials. Meanwhile, theoretical simulation based on density function theory (DFT) calculation provide available information to understand the Fenton-like catalytic mechanism on different exposed surfaces by modeling the interfacial adsorbate-adsorbent interactions. While during the optimizing process, the water molecule and other possible co-existing ions such as Cl^- and Na^+ in solution are generally neglected.[59] In order to make the simulation consistent with the experimental solution environment, self-consistent reaction fields with the solvent model density (SMD) model are suggested to be employed.[60, 61]

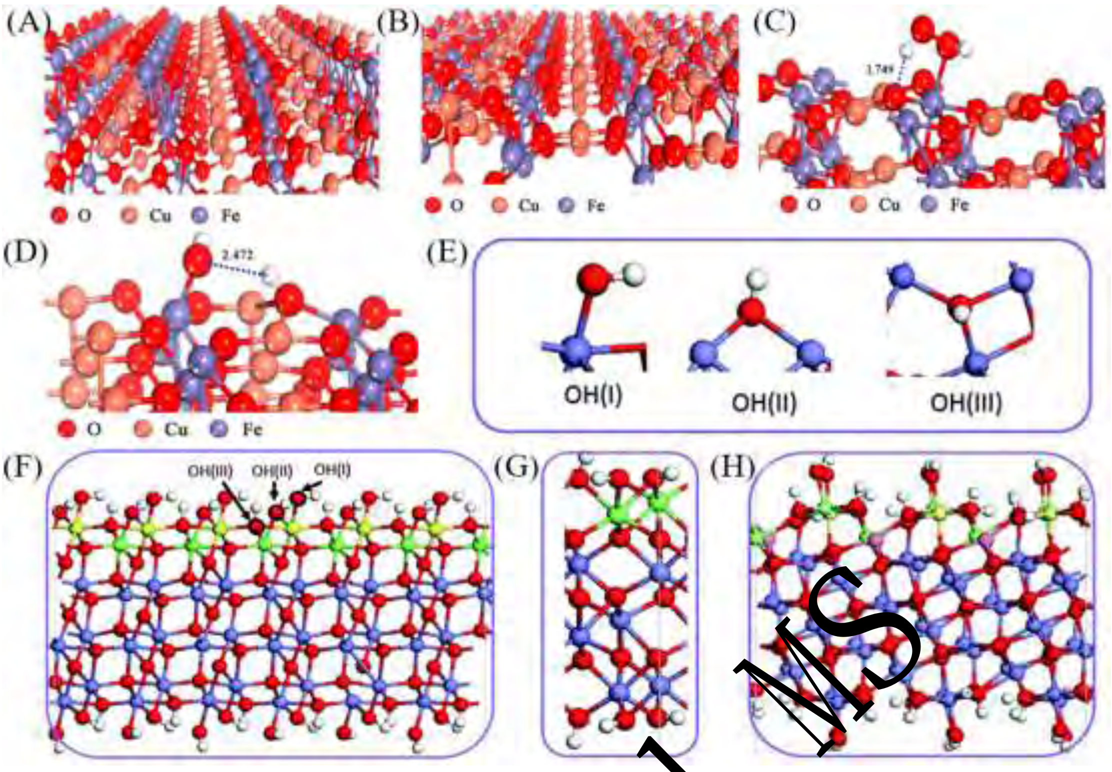

Figure 1 Optimized surface structures of (A) $CuFeO_2$ (012) and (B) $CuFeO_2$ (110); (C) H_2O_2 adsorption on $CuFeO_2$ (012) and (D) H_2O_2 adsorption on $CuFeO_2$ (110). Reprinted with permission from ref. 33, Copyright 2018, American Chemical Society; (E) Schematic drawing of singly, doubly and triply terminating OH groups, where O is in red, H is in white and other color represent Fe atoms; (F) Side views of optimized α-Fe_2O_3 (104) surfaces, where top-layer Fe atoms are in two groups highlighted by yellow and green color; (G) Side views of optimized α-Fe_2O_3 (001) surfaces, where top-layer Fe atoms are in green; and (H) Side views of optimized α-Fe_2O_3 (113) surfaces, where top-layer Fe atoms are in four groups highlighted by yellow, blue, pink and green, respectively. Reprinted with permission from ref. 38, Copyright 2015, Royal Society of Chemistry.

2.2 Defects

Defect engineering of Fe catalysts has also been proven as an effective strategy to fine-tune the Fenton-like catalytic performance since the existence of defects can usually modify the surface electronic structure, improve the charge transfer, or act as the active sites for H_2O_2 activation.[11, 39] Generally speaking, defects in Fe catalysts can be classified into two major categories, that is, dopants and vacancy.[12]

For element doping, the doped atoms may substitute the position of original atoms or enter into the interstitial void, and most probably, acting as active sites for H_2O_2 activation or resulting in variation of electron distribution owing to the different properties such as electronegativity between doped atoms and original atoms.[62-64] Taken S-doped $CoFe_2O_4$ as example, it can be found that the charge density of Fe-S bond and Co-S bond increased after S-doping (Fig. 2(A-B)), this would facilitate the redox cycle between surface Fe^{3+}/Fe^{2+} and Co^{3+}/Co^{2+}, leading to the existence of more Fe^{2+} and Co^{2+}. In this regard, sufficient •OH could be generated with adding a small amount of H_2O_2, and contributed to the efficient pollutant degradation.[65] Likewise, Panjwani et al. revealed that the higher electronegativity of Fe in comparison with Mn led to the electron transfer from Mn atoms to Fe atoms through Fe-O-Mn bond, then electron-poor center was formed around Mn and electron-rich center was formed around Fe in Fe-Mn-SiO_2. This unique electron structure thus facilitated H_2O_2 activation and reactive species generation.[66] Meanwhile, the nonuniform distribution of surface electrons caused by doping metal ions with lower oxidation states may also result in the generation of oxygen vacancies, ascribing to the charge compensation effects.[67, 68] For example, Soltani et al. reported that the oxygen vacancies concentration increased when increasing the doping amount of Ba in $Bi_{1-x}Ba_xFeO_3$, and the mechanism was related to the neutralization of charges produced by lower-valence Ba^{2+} substituting Bi^{3+}.[69]

In fact, oxygen vacancies as another crucial defect in Fe catalysts have also attracted an explosion of research interest in Fenton-like catalysis. As is well-known, oxygen vacancies are the most common anion vacancies in Fe oxide or Fe-based LDHs, and most recent studies have demonstrated the positive role of oxygen vacancies in promoting Fenton-like catalytic activity.[11, 41, 70, 71] On the one hand, it is reported that the oxygen vacancies with abundant localized electrons and coordinative unsaturated nature can significantly promote the adsorption of H_2O_2 molecule.[72, 73] Meanwhile, the interaction of oxygen vacancies with H_2O_2 usually result in the suitable elongation of O-O bond, therefore benefitting the subsequent H_2O_2 activation process.[40, 41] Taken the hollow sphere $CuFe_2O_4$ containing oxygen vacancies (HS $CuFe_2O_{4-\sigma}$) as example, H_2O_2 would be absorbed onto $Fe^{III}_{0.5}Cu^{II}_{0.5}$ sites on $CuFe_2O_4$ surface and oxygen vacancies sites on HS $CuFe_2O_{4-\sigma}$ surface with adsorption energy to be -0.558 eV and -5.982 eV, and O-O bond length to be 1.524 Å and 2.353 Å, respectively (Fig. 2(C-F)). As a result, HS $CuFe_2O_{4-\sigma}$ exhibited better Fenton-like activity than $CuFe_2O_4$.[11] On the other hand, the localized electron adjacent to oxygen vacancies are more likely to migrate, which can accelerate surface Fe^{3+}/Fe^{2+} redox cycle and promote H_2O_2 activation to generate •OH.[12, 74] More importantly, previous works have shown that the existence of oxygen vacancies is possible to reduce the coordination number of nearby metal sites.[75, 76] For instance, Wang et al. revealed that the Fe-O coordination number (3.4) in 2D Fe_3O_4 containing ample oxygen vacancies was lower than that in commercial Fe_3O_4 (4.6).[77] This will correspondingly affect Fenton-like catalytic performance since the coordination number of surface Fe sites are closely related to the H_2O_2 adsorption and activation process.[30, 51] Except for oxygen vacancies, the promoting effects of some other anion vacancies (i.e., sulfur vacancies in Fe sulfide) on Fenton-like process have also been reported with similar mechanism to oxygen vacancies.[78-80]

From the above all, it can be reckoned that the presence of defects is possible to promote Fenton-like reaction through creating a strong synergistic effect. Nevertheless, it should be emphasized that excessive defects may result in the deterioration of structural stability and electrical conductivity, and even lead to the structural collapse.[67] Therefore, it is significant to introduce a proper content of defects to regulate the surface structures such as surface atom coordination and electron distribution of Fe catalysts for improved Fenton-like performance.

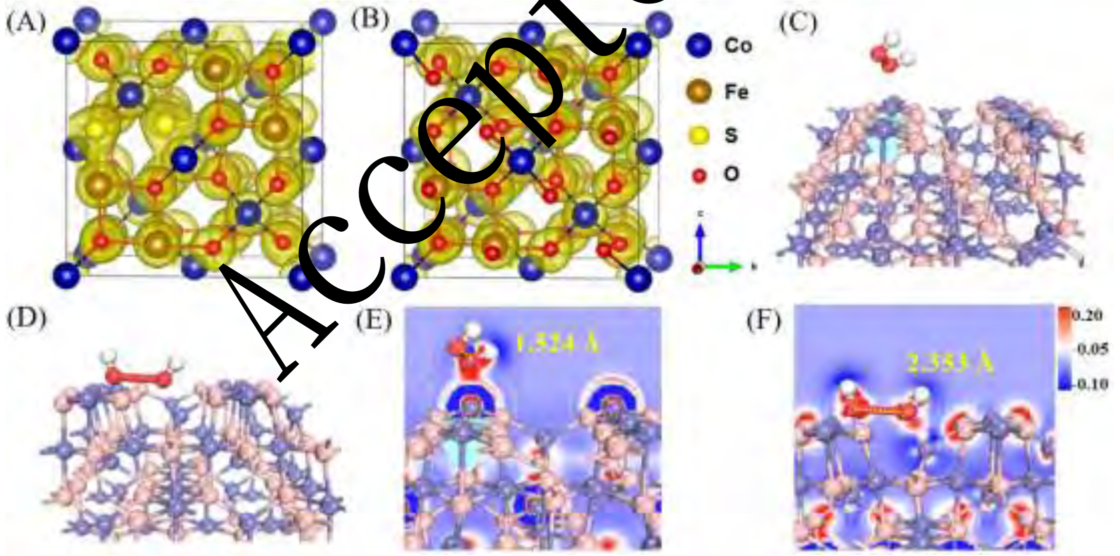

Figure 2 Charge density diagrams of (A) S-$CoFe_2O_4$ and (B) $CoFe_2O_4$; Reprinted with permission from ref. 65, Copyright 2021, Elsevier; Optimized geometry of absorption structure of H_2O_2 on (C) $CuFe_2O_4$ (110) $Fe^{III}_{0.5}Cu^{II}_{0.5}$ site, and (D) $CuFe_2O_{4-\sigma}$ (110) oxygen vacancies site; Charge density of H_2O_2 on (E) $CuFe_2O_4$ (110) $Fe^{III}_{0.5}Cu^{II}_{0.5}$ site,

and (F) $CuFe_2O_{4-\sigma}$ (110) oxygen vacancies site. The purple spheres at the tetrahedral position and octahedral position denote the composition of Fe and $Fe_{0.5}Cu_{0.5}$, respectively, and red and white spheres represent O and H atoms, respectively. Reprinted with permission from ref. 11, Copyright 2021, Elsevier.

2.3 Catalyst size

The size of Fe catalysts is also considered as a crucial factor for determining H_2O_2 activation performance and reactive species generation, which can be explained by the clear correlation between catalyst size and utilization efficiency of active sites.[37, 81] To be specific, larger catalysts particles may possess uneven aggregation of hundreds or thousands of metal atoms, and only a small fraction of them on the surface are exposed to reactants. When decreasing the particles size, the fraction of active atoms (on the surface) in the total number of atoms can be significantly increased due to fewer atoms aggregated together.[36, 37, 82, 83] The exposure of active sites to reactants could thus be increased, leading to higher active sites utilization efficiency. In this regard, compared to Fe catalysts with sizes of nanoparticles and nanoclusters, single Fe atoms can achieve highest utilization of metal active sites and then attain ultra-high activities.[84] Nevertheless, single metal atoms have high surface free energy, which are likely to aggregate during preparation process. Therefore, appropriate supports such as carbon substrates, g-C_3N_4, and metal oxides are typically required to stabilize single metal atoms by forming strong bonds.[82, 85, 86] For example, Yin et al. found that confined space and Si-OH groups of SBA-15 contributed to the successful formation of single Fe atom sites, where Fe atoms could substitute H atoms of Si-OH to form Fe-O bond for stabilization. Benefitting from the maximized atomic utilization, SAFe-SBA exhibited much higher Fenton-like degradation rate of phenol (100% in 90 min) than that of SBA-15 loaded α-Fe_2O_3 (80.3% in 180 min).[87]

Except for highest utilization of metal active sites, the unsaturated coordination environment and unique electronic structure of reactive sites in single atom catalysts (SACs) also benefit the improvement of catalytic activity.[81, 82, 88] For instance, some studies proposed that N atoms in the support materials could mightily anchor individual metal atoms to form metal-N coordination, the strong interaction between metal sites with neighboring pyridinic-N or pyrrolic-N then influenced the electron density of single-atom metal sites, thereby affecting the charge transfer between metal and H_2O_2 molecule.[89, 90] As shown in Fig. 3(A-B), Su et al. found that the atomic Fe-N_4 center was achieved in both carbon nitride loaded single Fe atoms (Fe_1/CN) and carbon nitride with abundant nitrogen vacancies loaded single Fe atoms (Fe_1-N_v/CN), and the adsorption edge position of Fe_1-N_v/CN was lower than that of Fe_1/CN, indicating the higher electron density of Fe sites in Fe_1-N_v/CN, which promoted H_2O_2 activation to generate •OH.[91] In another case, single Fe atoms could be anchored onto three-dimensional N-doped carbon nanosheets (Fe/NC) by forming Fe-N-C bond. During catalytic reaction, N atoms could attack electrons from the adjacent C atoms and transfer to the Fe atoms coordinated with them. This specific electronic configuration and electron-transfer process then led to the outstanding catalytic activity of Fe/NC.[92]

Nevertheless, the long-term stability of single atom catalysis come into question because the interaction between reactants and single atoms may weaken the interaction between support substrate and single atoms, and therefore resulting in the migration and aggregation of single atoms during reaction process if single atoms bound weakly to support.[90, 93] Taken the Pt atoms on Fe_3O_4 (001) surface as example, Bliem et al. found that Pt atoms agglomerated into sub-nanometer Pt clusters after adsorption of CO, since the formation of Pt(CO) species weakened the atom-support interaction and increased the mobility of Pt atoms.[94] Recently, some suitable and effective methods such as enhancing the metal-support interactions or confining the single metal atoms in limited space have been proposed to improve the stability of SACs during reaction.[37, 95, 96] Zuo et al. synthesized sandwich structure stabilized atomic Fe catalyst by anchoring single Fe atoms into g-C_3N_4-rGO support possessing double-layered structure. The stability of g-C_3N_4-Fe-rGO increased in comparison with g-C_3N_4-Fe, which could be ascribed to the fact that the double layer confined structure and extra Fe-O bond between Fe and rGO could further stabilize the atomically dispersed Fe sites.[97] Besides, it was also proposed that the strongly coordinated N-M bond produced from pyrolyzing MOFs endowed SACs with increased stability.[93, 98] According to above discussions, the development of atomic Fe catalyst brings new insights for enhancing Fenton-like catalytic activity. However, the application of single Fe atoms in Fenton-like process is still in infancy, it is significant to investigate the reaction process optimizing and the structure-catalysis relations in future studies.

2.4 Nanoconfinement

Nanoconfinement generally refers to the nanosized special restriction provided by catalysts.[99] As a novel nanotool, it has been employed in Fe-based heterogeneous

Fenton-like systems to minimize the mass transfer limitation. Some studies have proposed that under nanoconfined environment, the space where the reaction occurs is restricted, that is, the distance between "catalyst surface" and "reactants" will be controlled to a certain length scale. Then, the as-generated reactive species in close vicinity to target organic pollutant have more chances to attack these molecules, therefore benefiting the usage of the reactive species.[100-102] According to literature survey, the availability of reactive species, of which the concentration is strongly related to the diffusion distance can be greatly affected when varying the length scale of nanoconfinement.[103-105] Taken the degradation of para-chlorobenzoic acid by Fe_3O_4-anodized aluminum oxide (AAO) nanoreactor as example (Fig. 3(C-D)), the diffusion of •OH could be significantly minimized at a nanoconfined pore size below 25 nm. Consequently, the nanoreactors with smaller pore size achieved much higher degradation kinetic (i.e., 4.93×10^{-2} s^{-1} for nanoreactors$_{<20}$) than those with larger pore size (i.e., 6.4×10^{-3} s^{-1} for nanoreactors$_{200\text{-}300}$).[105]

In addition to reactive species utilization, controlling the length scale of nanoconfinement also provides an opportunity for interception of macromolecules and traverse of small molecule, thus achieving the selective degradation of target organic pollutant.[101, 106] During this process, the key factor is the quite different size between coexisted multicomponent organic pollutant and target organic pollutant. Furthermore, some other studies also proposed that confining Fe catalysts into carbon nanotubes (CNT) might bring novel insight into Fenton-like catalytic mechanism, because the curvature of CNT walls may give rise to the shift of π electron of graphene layers from the inner to outer surface and leads to the potential difference, therefore the nanoparticles confined inside CNT will exhibit different properties and chemical activities from those on the outer surface of CNT.[107, 108] For example, Guo et al. found that Fe_2O_3-out-CNT/H_2O_2 system without nanoconfinement would activate H_2O_2 to generate •OH, while $^1O_2$ was considered as the dominant reactive species in Fe_2O_3-in-CNT/H_2O_2 system under nanoconfinement, which might be explained by the interaction of generated HO_2•/•O_2^- with H_2O_2 or •OH within confined space (Fig. 3(E)).[109] The similar result was reported by Yang et al. using CNT for nanoconfinement (Fig. 3(F)).[110] All these research results provide useful guidance for employing nanoconfinement to enhance the Fenton-like performance of Fe catalysts.

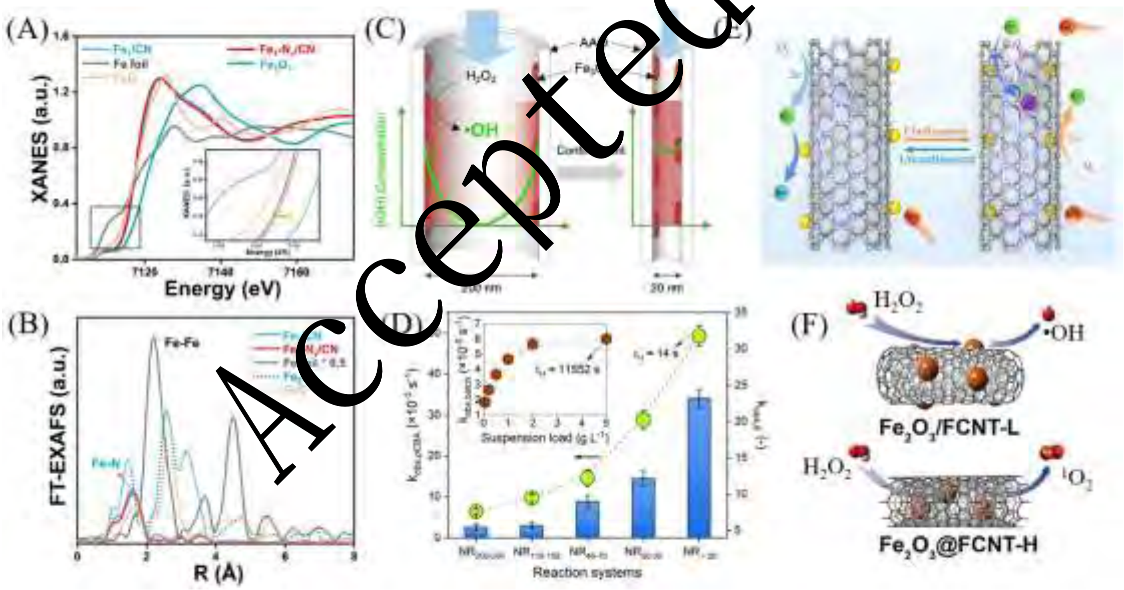

Figure 3 (A) Fe K-edge XANES spectra of Fe_1/CN, Fe_1-N_v/CN, standard Fe foil, FeO, and Fe_2O_3, and (B) Fourier-transformed (FT)-EXAFS curves at R space. Reprinted with permission from ref. 91, Copyright 2021, Wiley; (C) The diffusion of •OH in Fe_3O_4-AAO with different pore size, and (D) Pseudo-first-order rate constants in the nanoreactor series (left y-axis). Reprinted with permission from ref. 105, Copyright

2020, American Chemical Society; (E) Possible reaction mechanism in Fe_2O_3-in-CNT/H_2O_2 system and Fe_2O_3-out-CNT/H_2O_2 system. Reprinted with permission from ref. 109, Copyright 2021, American Chemical Society; (F) Illustration of possible mechanism in Fe_2O_3@FCNT-L/H_2O_2 system and Fe_2O_3@FCNT-H/H_2O_2 system. Reprinted with permission from ref. 110, Copyright 2019, PNAS;

3 Characterization technologies to determine structure properties

After understanding the impacts of structure properties on the Fenton-like catalytic performance, it is essential to introduce the characterizations technologies which can evaluate the achievements of structure design. The obtained information is helpful for understanding the structure-activity relationship, and providing a basic guide for rational structure design. Therefore, in this section, we will summarize some common characterization techniques for examining the above structure properties (Table 1).

Table 1 Summary of characterization technologies to determine structure properties.

Characterization techniques	Structure properties	Detailed information	References
SEM/TEM	Catalysts size (nanoparticle and nanoclusters), Nanoconfinement	Morphology in the nanoscale range	46, 55, 111
HR-TEM	Exposed surface	Lattice parameters	55, 112
HAADF-STEM	Catalysts size (single atom), Nanoconfinement	Morphology in the sub-angstrom range, visual confirmation of atom distribution	97, 109, 113
STM	Catalysts size (single atom)	Atomic sites and corresponding electronic structures	114-116

EDX-mapping	Defects	Surface elements composition	117, 118
XRD	Exposed surface	Crystal structure, peak intensity	38, 119
XPS	Defects, Nanoconfinement	Surface elements composition, chemical state of elements near the surface	11, 110, 120
XAS	Defects, Catalysts size (single atom)	The local bonding environments, (i.e., coordination number, interatomic distance), chemical states of specified elements	121-123
EPR	Defects	Fingerprinting information about the unpaired electrons	71, 124
N_2 adsorption-desorption isotherms	Nanoconfinement	Brunauer-Emmet-Teller (BET) surface area and pore volume	125, 126

3.1 Characterization techniques for exposed surface

Typically, transmission electron microscopy (TEM) characterization can be used to identify the exposed surface of materials based on information about lattice parameters.[46, 127] Taken the Fe_3O_4 nanoparticles as example, a lattice spacing of 0.486 nm could be observed in the high-resolution TEM (HR-TEM) image of Fe_3O_4 nano-octahedrons (Fig. 4(A)), which was close to the (111) planes of Fe_3O_4. Meanwhile, the corresponding Fast Fourier Transform (FFT) image was closely related to the diffraction from the crystal planes of Fe_3O_4, all of this information suggested that Fe_3O_4 nano-octahedrons was mainly enclosed by (111) planes.[55] In another case, the HR-TEM image and corresponding FFT pattern confirmed that $FeWO_4$-010 nanosheets and $FeWO_4$-001 nanosheets were predominantly exposed with (010) surface and (001) surface, respectively.[112]

Apart from HR-TEM, X-ray diffraction (XRD) can also provide useful information to confirm the major exposed surface of materials. In general, XRD is an analytical tool for investigating crystalline structure, each diffraction peak in XRD pattern corresponds to a different crystal facet of materials,[51, 112] and its relative peak intensity has positively relationship to the extent of crystal facet exposing.[50, 55] For instance, in the XRD pattern of MnO_2 with different exposed surface (Fig. 4(B)), the peak intensity corresponding to (110) surface was the strongest among the diffraction peaks in (310), (110), and (100) when MnO_2 was mainly exposed with (110) surface.[119] Chan et al. also reported that the variation of peak intensity of (104) peak and (110) peak in the XRD pattern of α-Fe_2O_3 rhombohedron, hexagonal bipyramid, and hexagonal nanoplate can be ascribed to the morphology transformation.[38] However, it should be noted that it is inaccurate to determine the exposed surface of material by XRD analysis alone, it is usually required to combine with TEM analysis.

3.2 Characterization techniques for defects

As mentioned earlier, the defects in Fe catalysts are generally classified into two main categories, that is, dopants and vacancy. For dopants, the corresponding X-ray photoelectron spectrometry (XPS) spectrum, Fourier transform infrared spectra (FTIR) spectra, and Energy dispersive X-ray (EDX) mapping can be used to verify its existence through clarifying the element composition and chemical bond.[117, 118, 128]

In the case of vacancies, XPS is a common technology to demonstrate its existence in nanomaterials since the generated vacancies usually leads to the change of chemical environments of corresponding elements, which can be reflected by XPS peaks.[69, 129] Taken the oxygen vacancies as example, Zhang et al. reported that the O 1s XPS spectrum in Co doped $ZnFe_2O_4$ can be divided to two peaks including lattice oxygen (529.6 eV) and surface oxygen (530.9 eV). After Co doping, the lattice oxygen peak intensity of $ZnFe_{0.8}Co_{0.4}O_{2.4}$ obviously decreased and the corresponding binging energy shifted by 0.3 eV in comparison with pure $ZnFe_2O_4$ (Fig. 4(C)), indicating that formation of oxygen vacancies.[120] This phenomenon can also be found in O 1s spectrum of Ca-Fe_2O_3, hollow sphere $CuFe_2O_4$ [11], Fe_3O_4,[130] and alkylpolyglycoside modified $MnFe_2O_4$.[131]

Meanwhile, X-ray absorption spectroscopy (XAS) based on synchrotron radiation has emerged as another crucial approach to directly identify the existence of vacancies in material.[120, 132] XAS can study the local atomic structure in a material, such as the changes in electronic structures and geometry, which can be classified to X-ray absorption near edge structure (XANES) and extended X-ray absorption fine structure (EXAFS) depending on the absorption energies, in which XANES usually provides information about the oxidation state of the absorbing atom, and EXAFS generally determines the local bonding environments of the absorbing atom, such as atomic coordination number and interatomic distance.[133, 134] Typically, as revealed by the Fourier transform (FT) EXAFS spectra at W L_3-edge, defect-rich WO_3 (R-WO_3) showed shifted peaks and lower peak intensities in comparison with commercial WO_3

(C-WO_3) and defect-deficient WO_3 (D-WO_3), manifesting their distinguishing local atomic arrangements (Fig. 4(D)). Besides, R-WO_3 displayed a reduced coordination number compared to C-WO_3 and D-WO_3, which demonstrated that abundant oxygen vacancies were formed in R-WO_3.[135] Xiao et al. also compared the coordination number of Co in pure Co_3O_4 and Co_3O_4 etched by Ar plasma (V_o-Co_3O_4) via observing the FT-EXAFS spectra at Co k-edge, where the relatively lower coordination number was found in the later, indicating the creation of oxygen vacancies after etching Co_3O_4 with Ar plasma. In addition, by studying the Co K-edge XANES spectra, it was found that the Co valence in V_o-Co_3O_4 decreased comparing to pure Co_3O_4, further identifying the existence of oxygen vacancies in V_o-Co_3O_4.[123]

Besides the above technologies, Electron paramagnetic resonance (EPR) characterization is also a common approach to verify the vacancy in materials since there are usually some unpaired electrons around the vacancy.[124, 129, 136] Moreover, it is also possible to compare the concentration of vacancies by studying the change of EPR signal.[124] For example, Wu et al. found that all Fe-Co LDH samples prepared with different precursor proportions showed EPR signals with g value of 2.002, demonstrating the presence of oxygen vacancies. Besides, the EPR intensities varied when the content of Fe precursor increased, which revealed the variation of amount of oxygen vacancies (Fig. 4(E)).[71] Liu et al. also verified the existence of sulfur vacancies in Fe_3S_4 by EPR technology with g value of 2.005.[80]

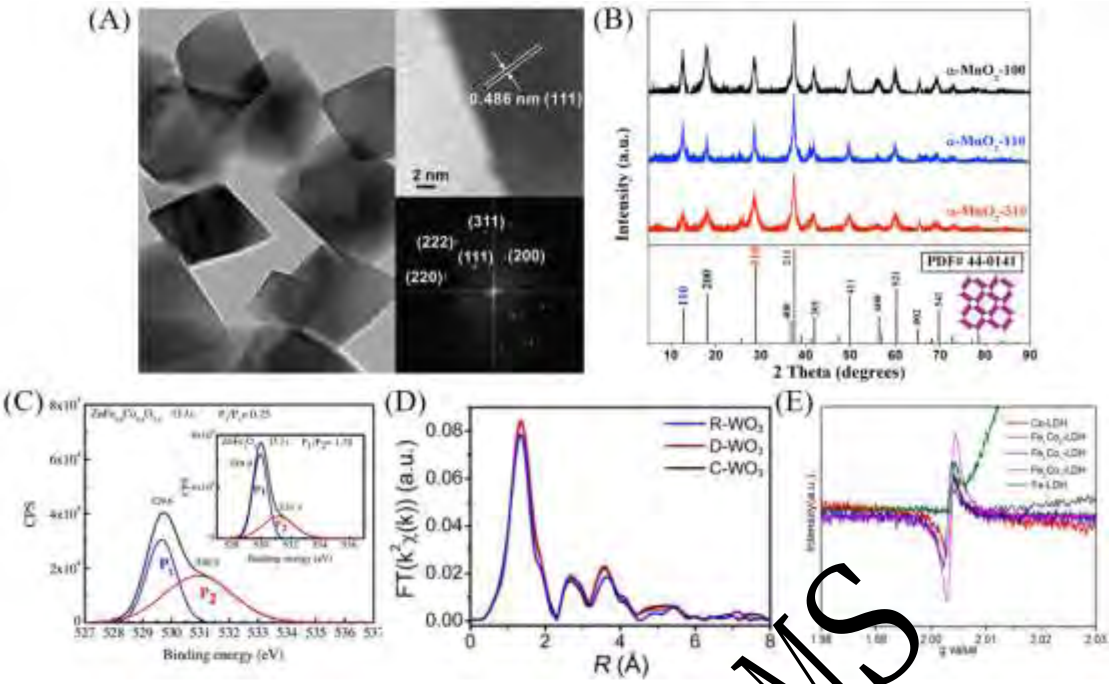

Figure 4 (A) TEM, HRTEM images (upper right insets), and Fourier transforms images (lower right insets) of Fe_3O_4 nano-octahedrons. Reprinted with permission from ref. 55, Copyright 2017, American Chemical Society; (B) XRD patterns of α-MnO_2 with different exposed facets. Reprinted with permission from ref. 119, Copyright 2018, American Chemical Society; (C) O 1s XPS spectra of $ZnFe_{0.8}Co_{0.4}O_{2.4}$ (the insert shows the O 1s XPS spectra of $ZnFe_2O_4$). Reprinted with permission from ref. 120, Copyright 2020, Elsevier; (D) Fourier-transform W L_3-edge EXAFS spectra of the samples in reference to commercial WO_3. Reprinted with permission from ref. 135, Copyright 2016, American Chemical Society; (E) EPR spectra of the synthesized LDHs. Reprinted with permission from ref. 71, Copyright 2020, Elsevier.

3.3 Characterization techniques for catalyst size

As common technologies to observe the morphology of materials, SEM and TEM characterizations have been widely employed to study the approximate size of catalysts.[50, 55, 137] For example, it can be observed from Fig. 5(A) that the α-Fe_2O_3

rhombohedron exhibited uniform size with an edge about 50 nm.[46] Nevertheless, the resolution of conventional SEM and TEM technologies at nanoscale cannot provide information at the atomic scale. For more detailed information about SACs, some other characterizations such as aberration-corrected high-angle annular dark-field imaging scanning TEM (HAADF-STEM), Scanning tunneling microscopy (STM), and XAS are further required.[81, 87, 113]

To be specific, HAADF-STEM is possible to provide visual confirmation of spatial distribution and location of single metal atoms over catalyst surface owing to its resolution in sub-angstrom scale, therefore identifying the individual atoms.[87, 89, 97] For example, the distribution of isolated Fe atoms over carbon surface can be directly observed from enlarged HAADF-STEM images of N-doped porous carbon anchored single Fe atoms (Fe SA/NPCs) (Fig. 5(B)).[113]

As another surface analytical technology that enables imaging of the morphology of surfaces and mapping the distribution of electronic density, STM has also been employed for characterizing SACs with two-dimensional structure.[114-116] Furthermore, the theoretical simulation based on STM image could provide more detailed information about atomic sites and change of electronic structures.[81] Taken the graphene confined single iron catalyst (FeN_4/GN) as example, the simulated STM images in Fig. 5 (D) showed that the C and N atoms adjacent to Fe center were electronically richer compared to C atoms located farther away, which was consistent with the measured low-temperature STM image (Fig. 5(C)), where Fe center was resolved to a bright spot, and the neighboring atoms appeared brighter than other C atoms of graphene matrix.[115]

XAS is also a common technology to identify the single metal atoms in recent studies.[121, 122] In general, no metal-metal bonds form in the structure of SACs, which can be reflected by the bonding information (i.e., bond length and coordination number) obtained from EXAFS fitting results.[81, 86, 89] For example, the FT-EXAFS fitting curves of Fe SA/nitrogen-doped porous carbon showed a dominant peak at approximately 1.5 Å, corresponding to the Fe-N scattering paths. Besides, the Fe-Fe peak at ~2.2 Å was not found. Moreover, the fitting results also revealed that the coordination number of Fe was about 4.4, which indicated the presence of Fe-N_4 coordination with some wobbling effect of a fifth ligand.[113] In addition, the valence state of single metal atoms can be revealed by XANES analysis.[113, 122]

3.4 Characterization techniques for nanoconfinement

In general, the SEM and TEM characterizations may provide useful information to confirm the specifical nanoconfinement through showing the distribution of particles.[138, 139] For example, The SEM and TEM images of FeCu-N/C confirmed the distribution of some metal nanoparticles at the top and inner walls of CNT.[111] The HAADF-STEM images of Fe_2O_3-in-CNT and Fe_2O_3-out-CNT also clearly showed that Fe_2O_3 distributed inside and outside CNT, respectively (Fig. 5(E-F)).[109] Besides, N_2 adsorption-desorption isotherms, which is generally employed to investigate the pore characteristics and specific surface areas of a material,[140] can also confirm the spatial nanoconfinement of nanoparticles. In general, confining nanoparticles in the internal pores of porous materials probably lead to the decrease of Brunner-Emmet-Teller (BET) surface area and pore volume owing to the part blockage of the pore system.[141, 142] For example, the confinement of Pd/PdO/Fe_2O_3 nanoparticles in the SBA-15 was probed by the variation of pore volume and BET surface area. The results indicated that pure SBA-15 and FePd-SBA showed similar hexagonal pore structure, while the pore volume and surface area decreased from 0.94 cm^3/g and 558 m^2/g for pure SBA-15 to 0.55 cm^3/g and 369 m^2/g for FePd-SBA, respectively, which could be ascribed to the successful incorporation of FePd nanoparticles inside SBA-15 pore channels.[125] Lu et al. also revealed the lower BET surface area and pore volume of γ-Fe_2O_3/ordered mesoporous carbon in comparison with bare ordered mesoporous carbon, which can be related to the immobilization of γ-Fe_2O_3 into the pore system.[126]

Apart from the above technologies, the confinement of nanoparticles may also be proved by XPS, since XPS is a surface analysis method which can obtain the information from surface at a depth about 3-5 nm.[102, 143] For example, Yang et al. found that the mass fractions of Fe_2O_3 in Fe_2O_3/FCNT-H (Fe_2O_3 anchored inside CNT for nanoconfinement) and Fe_2O_3/FCNT-L (Fe_2O_3 dispersed on the outer surface of CNT) were detected to be similar, while the peak intensities of Fe 2p for Fe_2O_3/FCNT-H was much lower than that for Fe_2O_3/FCNT-L (Fig. 5(G)), which was possibly because the limited probe depth of the photoelectrons made it difficult to detect the Fe_2O_3 inside the CNT.[110]

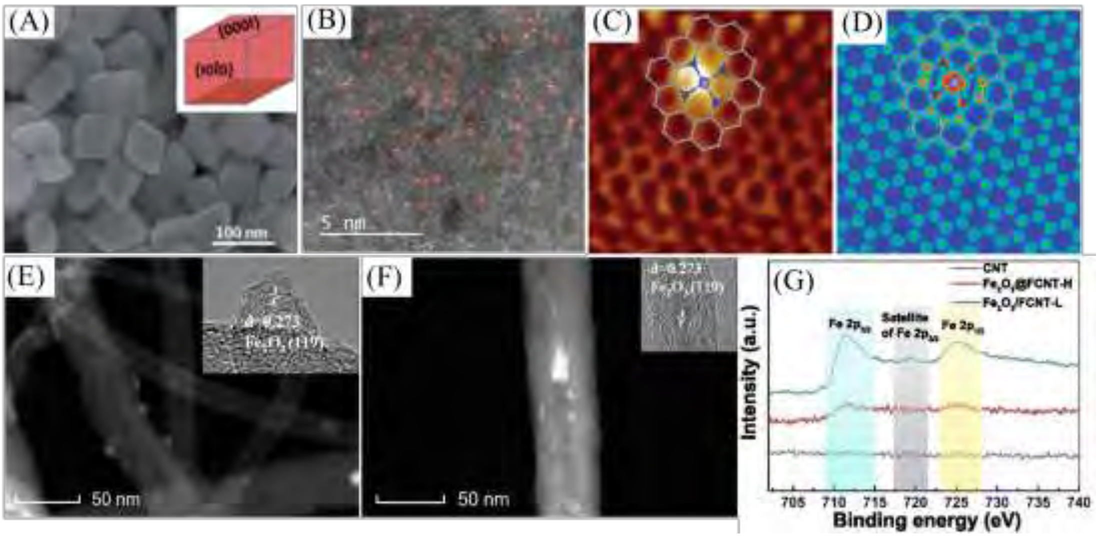

Figure 5 (A) SEM images of α-Fe_2O_3 rhombohedron with exposed (0001) and $(10\bar{1}0)$ facets. Reprinted with permission from ref. 46, Copyright 2013, The Royal Society of Chemistry; (B) The enlarged HAADF-STEM image of Fe SA/NPCs. Reprinted with permission from ref. 113, Copyright 2022, Wiley; (C) Low-temperature STM image of FeN_4/GN-2.7 and (D) Simulated STM image for (C). The inserted schematic structures represent the structure of the graphene-embedded FeN_4. The gray, blue, and light blue balls represent C, N, and Fe atoms, respectively. Reprinted with permission from ref. 115, Copyright 2015, American Association for the Advancement of Science; (E) HADDF-STEM image of Fe_2O_3-out-CNT and (F) Fe_2O_3-int-CNT (Inset is the HRTEM image of the Fe_2O_3 nanoparticle). Reprinted with permission from ref. 109, Copyright 2021, American Chemical Society; (G) Fe 2p XPS spectra of CNT, Fe_2O_3/FCNT-L and Fe_2O_3@FCNT-H. Reprinted with permission from ref. 110, Copyright 2019, PNAS.

4. Structure design of iron catalysts

After fully understanding the impacts of the structure properties on the Fenton-like catalytic performance, and technologies to determine structure-activity relationship, we will then focus on the methods to prepare Fe catalysts with specific structure. Generally speaking, the catalysts structures will be greatly affected by the changes of synthesis parameters, such as temperature, solvent, and precursor. Therefore, in this section, we review some frequently-used strategies for modulating exposed surface, creating defect, adjusting catalyst size, and designing nanoconfined environment, which is significant for endowing Fe catalysts with desirable Fenton-like catalytic properties.

4.1 Design of exposed surface

For preparing Fe catalysts with well-defined special surface, many efforts have been devoted. Generally, the final exposed surface of crystal are intrinsically determined by the growth rate and orientation of seeds that relate to the interplay between growing thermodynamics and kinetics.[144, 145] Under thermodynamic control, the greatest proportion of the produced product will be the most stable product, that is, the final crystal is generally enclosed by the surface possessing low surface energy to minimize the total surface energy of crystal, and keep the crystal in an equilibrium shape.[119, 146] While the surfaces with high surface energy are likely to vanish in the crystal owing to the fast growth rate.

In contrast, the relative growth rate of different surface could be regulated under kinetic control, such as changing the synthesis parameters or using morphology-capping agents (i.e., oxalic acid, hydrofluoric acid, phosphate ions),[50, 146, 147] and thus, it is possible to synthesize same crystal with different exposed surface. For example, Fe_3O_4 nanoparticles with different exposed surface, namely, nanocubes with (100) surface and rhombicuboctahedral with both (100) and (110) surfaces, were synthesized by controlling the concentration of precursor or injection rate of precursor.[148] In another study, phosphate ions ($H_2PO_4^-$) as morphology capping agents could allow the etching to proceed along (001) direction through adsorbing on the (110) planes of α-Fe_2O_3 crystal, thereby acquiring α-Fe_2O_3 nanodiscs with major (001) facets and minor (110) facets (Fig. 6(A)).[149] It is worth noting that the select of morphology-capping agents is crucial to control the surface energies and surface growth in the crystal due to their reaction with specific surface. Theoretically studying the variation of surface energy of a surface before and after adsorbing morphology-capping agents may provide a promising opportunity for choosing an appropriate morphology-capping agent to synthesize crystalline Fe catalysts with target surface,[54, 150] which needs more research focus in the future.

4.2 Design of defect

As previous mentioned, dopants and vacancy are the two major defects in Fe catalysts. For preparing Fe catalysts with dopants, the raw materials of dopants and Fe catalysts are generally mixed homogeneously to form a precursor, following by hydrothermal or calcination treatment of the precursor to form doped Fe catalysts.[62, 64, 117]

For preparing Fe catalysts with oxygen vacancies, various methods including thermal treatment, element doping, and reduction processing been developed.[68, 124, 151] Among them, thermal treatment has been widely applied. It is demonstrated that calcining Fe catalysts in an inert or vacuum atmosphere at high temperature could result in the removal of lattice oxygen without phase transformation, leading to the generation of oxygen vacancies. For example, plentiful oxygen vacancies could be introduced into $LaFeO_3$ through annealing $LaFeO_3$ in a hydrogen atmosphere (0.95 bar), and the oxygen vacancies concentration increased with increasing the annealing temperature.[152] Moreover, Ling et al. found that oxygen vacancies could be created on hematite by sintering hematite under oxygen-deficient atmosphere (the mixture of N_2 and air). Besides, the oxygen content during thermal treatment prominently influenced the production of oxygen vacancies.[153] In another case, Xiong et al. synthesized a α-Fe_2O_3 nano-octahedron with oxygen vacancies through two-step calcination of Fe-MOF precursor. During the calculation process, Fe-MOF was firstly oxidized to α-Fe_2O_3 under air atmosphere, and the α-Fe_2O_3 with oxygen vacancies was obtained by further calcining the obtained α-Fe_2O_3 under nitrogen atmosphere (Fig. 6(B)).[154]

Besides that, element doping is also considered to be an effective technology for introducing oxygen vacancies into Fe catalysts. Many literatures have reported that the oxygen vacancies could be formed via doping metal ions with lower oxidation states due to a charge compensation effect, and the mechanism can be explained by Eq. 3.[68, 155, 156] For instance, in Xie et al.'s work of using Cu-doped Fe_3O_4@γ-Al_2O_3 to initiate Fenton-like reaction, the substitution of Fe^{3+}/Al^{3+} by low-valent Cu^{2+} could lead to the metal valence state transformation, and oxygen vacancies were generated to meet the charge balance requirement, which benefited the activation of H_2O_2 to generate •OH.[157] In another case, Zhao et al. prepared a novel nickel-substituted $AgFeO_2$ ($AgFe_{1-x}Ni_xO_2$) catalyst with controlled oxygen vacancies through hydrothermal method. The results demonstrated that Ni^{2+} with lower valence substituted the Fe^{3+} in the B-site of delafossite structure, and therefore leading to the generation of abundant oxygen vacancies.[156] Zhao et al. also found that the increased concentration of oxygen vacancies in Fe/CeO_2 composite could be ascribed to the substitution of framework Ce^{4+} by Fe^{3+} with a lower oxidation state.[158] In addition, doping metal ions with larger atomic radius may also lead to the generation of oxygen vacancies. As literatures reported, doping metal ions with much larger atomic radius might cause the partial replacement of strongly-bound oxygen by relatively weakly-bound oxygen, which tended to release into solution, and forming oxygen vacancies.[64, 159] For example, Tian et al. revealed that doping Ce into 3D Mn_2O_3 could successfully increase the concentration of oxygen vacancies because of the much larger atomic radius of Ce in comparison with Mn.[159]

$$2A^{n+}O \xrightarrow{B^{(n-1)+}O} 2A_B^{'} + V_O^{\cdot\cdot} + 2O_O^{\times} \qquad (3)$$

where A represented the bulk metal ions, B represented the doped metal ions, the superscript × represented nominal neutral charge, ' represented nominal negative charge, and $^{\cdot}$ represented nominal positive charge.

Some reports show that using reducing agents such as $NaBH_4$ during synthetic process can also introduce oxygen vacancies into Fe catalysts, and the mechanism is related to the charge neutralization arising from the decreased oxidation state of Fe during redox cycle.[76] For example, (Co, Fe)$_3$O$_4$/carbon cloth with massive oxygen vacancies was synthesized via immersing the obtained (Co, Fe)$_3$O$_4$/carbon cloth in the $NaBH_4$ solution for a period.[160] Yan et al. pointed out that treating the pristine $CoFe_2O_4$ hollow nanosphere with $NaBH_4$ solution could produce abundant oxygen vacancies on

$CoFe_2O_4$ surface.[161] Besides, the presence of reducing agents may also modulate the generation of sulfur vacancy. As some studies reported that altering the ratio of ethylene glycol with water during synthesis process was capable of adjusting the concentration of sulfur vacancy in Fe_3S_4.[80, 162]

4.3 Design of catalyst size

The size of catalyst can usually be modulated by changing the synthesis parameters (i.e., the ratio of precursors, pH of the growth solution, reaction temperature and reaction time).[52, 55, 163] For example, the γ-Fe_2O_3 with catalyst size from 2.0 to 12.0 nm were synthesized via increasing the solvothermal temperature from 130 to 250 °C (Fig. 6(C-G)).[164] In another case of microwave-assisted synthesizing Fe_3O_4, the particle size of Fe_3O_4 also changed when varying the microwave irradiation time.[55]

While for synthesizing SACs, it is paramount to limit the migration of isolated single atoms on the support materials. Many corresponding strategies such as constructing defects to trap metal precursors to stabilize the isolated metal atoms,[165] employing molecular-scale pores of porous materials (i.e., covalent-organic frameworks and MOFs) as cages to confine metal species and anchor single metal atoms,[82, 86] using coordinating atoms with lone pairs of electrons, for instance, S, N, and O on support materials to bind metal precursors and stabilize single metal atom,[97, 166] and freezing the homogeneous solution of metal precursors to limit the thermal motion of metal species[167] have thus been proposed in the field of SACs synthesis. Recently, some studies also proposed that pyrolyzing organic-Fe rich biomass, such as Spirulina and Enteromorpha, is possible to generate carbon-based SACs because of the presence of Fe-S or Fe-N bonds in their component,[168-170] which provides a facile and practical strategy for preparing SACs. Nevertheless, improving the metal loading content is still challenging in the field of SACs synthesis although the loading amount of single metal atoms is usually positively correlated to their catalytic activity. How to increase the metal atoms loading while avoiding the agglomeration arising from their high surface energy and high reactivity needs to be further solved.

4.4 Design of nanoconfined environment

In view of the particular advantageous of nanoconfinement effect for Fenton-like process, most efforts have also been devoted to preparing nanoconfined Fe catalysts. Diverse porous scaffolds with varying material composition such as carbon material (i.e., CNT, mesoporous carbon),[171, 172] metal oxides (i.e., TiO_2, anodized aluminum oxide),[173, 174] natural minerals (i.e., montmorillonite),[175] MOFs,[176] ceramic ultrafiltration membrane,[106] and silica,[125, 177] have been widely employed to encapsulate Fe oxides, zero-valent Fe or Fe complexes to provide nanoconfined environment through the formation of core@tube, core@shell, mesoporous or lamellar structures. Generally, hard-template method, soft-template method, and ship-in-a-bottle method are normally used for preparing core@shell structure.[178] The other three structures could be realized by immersing scaffolds with nanotube, mesoporous, or lamellar structures into Fe precursors, followed by calcination or centrifugation.

However, Fe ions may be existed on both external and internal surface of scaffolds, how to drive the diffusion of Fe ions into the nanoconfined channel of scaffolds should be taken into consideration in the process of preparing nanoconfined Fe catalysts. Wang et al. proposed a vacuum-assisted impregnation method for synthesizing TiO_2 nanotube confined Fe_2O_3 catalyst, in which the titanate nanotubes were added into $Fe(NO_3)_3$ aqueous solution and stirred under vacuum atmosphere ($p < 0.01$ Pa). In this case, the capillary effect that driven precursor solution into the internal pores of titanate nanotubes could be strengthened.[179] In another study of synthesizing Fe^0-in-CNTs, Su et al. promoted the diffusion of Fe ions into the nanoconfined channel through altering the precursors, reaction temperature and time (Fig. 6(H)).[171] All of these researches provide useful guidance for further development of confined Fe catalysts.

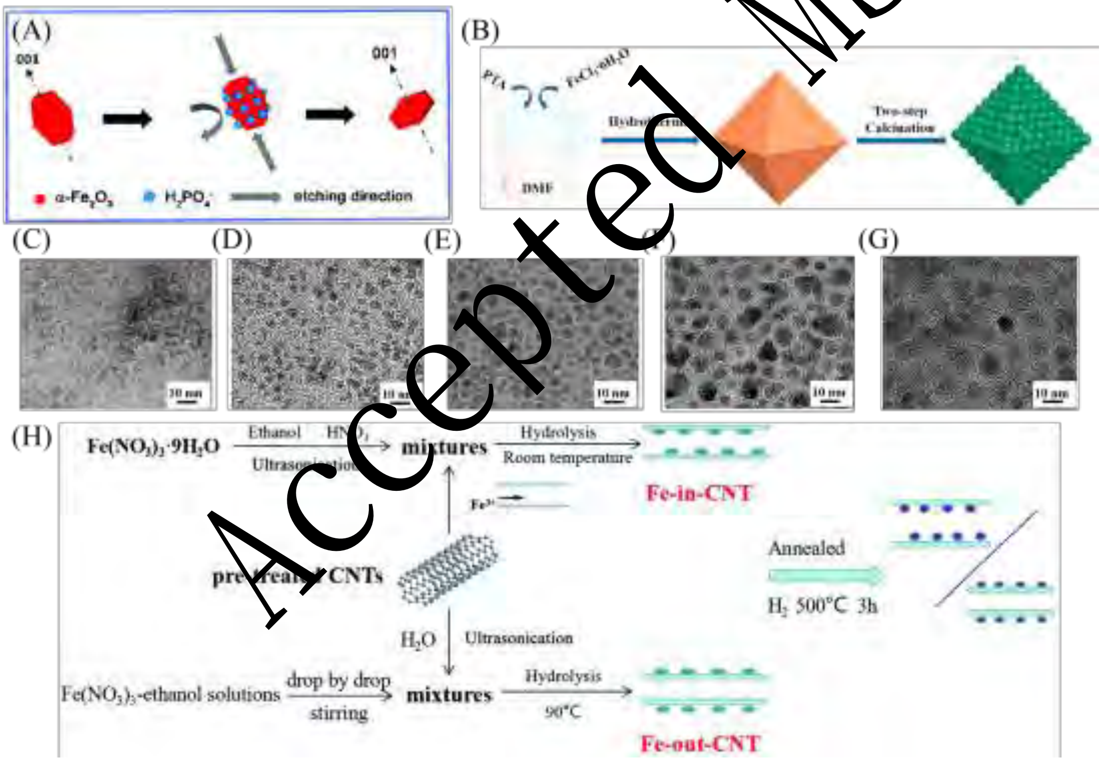

Figure 6 (A) Schematic illustration of the etching process. Reprinted with permission from ref. 149, Copyright 2010, American Chemical Society; (B) Schematic representation of the preparation process of oxygen deficient α-Fe_2O_3. Reprinted with permission from ref. 154, Copyright 2020, Elsevier; TEM images of the size-defined γ-Fe_2O_3: (C) γ-Fe_2O_3-130, (D) γ-Fe_2O_3-180, (E) γ-Fe_2O_3-200, (F) γ-Fe_2O_3-230, (G) γ-

Fe_2O_3-250. Reprinted with permission from ref. 164, Copyright 2010, Elsevier. (H) Experimental diagram showing the preparation of Fe^0-in-CNT and Fe^0-out-CNT. Reprinted with permission from ref. 171, Copyright 2019, The Royal Society of Chemistry.

5. Summary and Perspectives

Until now, heterogeneous Fenton-like process has been widely applied in wastewater treatment. Meanwhile, the nontoxicity of Fe, rich source of Fe, as well as structure flexibility of Fe catalysts have created many opportunities for actual application. In this case, heterogeneous Fenton-like process based on Fe catalysts have attracted considerable attention. However, the negative effects related to excessive use of H_2O_2 should not be overlooked. Therefore, it becomes more significant to understand structure-activity relationships to improve H_2O_2 utilization, and reducing consumption of H_2O_2 for environmentally sustainable application. In this review, we mainly focus on the fundamental and experimental advances in structure design of Fe catalysts for modulating the atomic and electronic structure to enhance Fenton-like performance. To be specific, modulating the structure properties of Fe catalysts (exposed facet, defects, catalyst size, and space confinement) is possible to facilitate the exposure of active sites, increase the electron density around active sites, alter coordination number, promote charge transfer or minimize mass transfer limitation, and therefore boosting the Fenton-like reaction. Besides, some characterization technologies for evaluating the achievements of structure design and synthetic strategies to design Fe catalysts with specific structure are also summarized. Based on the current studies, the existing challenges and further research suggestions are proposed.

Firstly, except for enhancing H_2O_2 utilization to reduce its consumption, structure design of Fe catalysts may also lead to the change of reaction mechanism, for example, the varied contribution of radical pathway and nonradical pathway. Therefore, it is worth studying the effects of structure design on catalytic mechanism. The obtained details may shed new light on Fe-based Fenton-like reaction.

Secondly, it is essential to understand the link between structure properties of Fe catalysts and their synthesis conditions more precisely. As described in this manuscript, a number of methods have been successfully employed to design exposed surface, defects, catalyst size, and nanoconfined environment, while structure design in a controllable manner remains a great challenge. To this end, the formation mechanisms of these structure properties need more elucidation, so that achieving controllable synthesis of Fe catalysts with specific structures.

Thirdly, the nature of the mentioned four structure properties to affect Fenton-like performance could be attributed to the variation of catalysts atomic and electronic structure, which have a significant influence on the interaction between catalysts and H_2O_2. Therefore, in addition to these structure properties, other modification strategies that can optimize coordination number, electron distribution and charge transfer can also be developed for construction of highly efficient Fe catalysts.

Fourthly, some other metal-based catalysts, for instance, Cu catalysts, Mn catalysts, Co catalysts, etc., are also widely used in heterogeneous Fenton-like system for organic pollutant degradation. The mentioned structure design strategies in this review can also be applied to design other metal catalysts for acquiring enhanced Fenton-like catalytic activity, thus promoting the development of environmental-friendly and sustainable materials for wastewater treatment.

Conflicts of interest

The authors declare that they have no known competing financial interests or personal relationships that could have appeared to influence the work reported in this paper.

Acknowledgments

This study was financially supported by the Program for the National Natural Science Foundation of China (U20A20323, 51521006, 51779090, 52170161, 51879101, 51579098, 51709101, 51809090, 51909084), the National Program for Support of Top-Notch Young Professionals of China (2014), the Program for Changjiang Scholars and Innovative Research Team in University (IRT-13R17), and Hunan Natural Science Foundation (2020JJ3009), Hunan Researcher Award Program (2020RC3025), Hunan Provincial Science and Technology Plan Project (2018SK20410, 2017SK2243, 2016RS3026), the Fundamental Research Funds for the Central Universities (531118010247, 531118040083), and the Science and Technology Innovation Program of Hunan Province (2021RC2057).

Reference

1. L. Qin, Z. Wang, Y. Fu, C. Lai, X. Liu, B. Li, S. Liu, H. Yi, L. Li, M. Zhang, Z. Li, W. Cao and Q. Niu, *J. Hazard. Mater.* 2021, **414**, 125448.
2. C. Lai, Z. An, H. Yi, X. Huo, L. Qin, X. Liu, B. Li, M. Zhang, S. Liu, L. Li, Y. Fu, X. Zhou, Z. Wang, N. An and X. Shi, *J. Colloid Interf. Sci.* 2021, **600**, 161-173.
3. B. Li, S. Yu, M. Zhou, C. Chen, C. Lai, M. Zhang and H. Lin, *J. Mater. Chem. A*, 2022, **10**, 3905-3932.
4. J. He, C. Lai, L. Qin, B. Li, S. Liu, L. Jiao, Y. Fu, D. Huang, L. Li, M. Zhang, X. Liu, H. Yi, L. Chen and Z. Li, *Chemosphere* 2020, **256**, 127083.
5. L. Jiang, Y. Liu, S. Liu, G. Zeng, X. Hu, X. Hu, Z. Guo, X. Tan, L. Wang and Z. Wu, *Environ. Sci. Technol.* 2017, **51**, 6352-6359.
6. C. He, W. Xia, C. Zhou, D. Huang, C. Zhang, B. Song, Y. Yang, J. Li, X. Xu, Y. Shang and L. Du, *Chem. Eng. J.* 2022, **430**, 132751.
7. M. Zhang, C. Lai, B. Li, F. Xu, D. Huang, S. Liu, L. Qin, Y. Fu, X. Liu, H. Yi, Y. Zhang, J. He and L. Chen, *Chem. Eng. J.* 2020, **396**, 125343.
8. B. Li, C. Lai, H. Lin, S. Liu, L. Qin, M. Zhang, M. Zhou, L. Li, H. Yi and L. Chen, *Chem. Eng. J.* 2022, **431**, 134044.
9. Y. Fu, Z. Yin, L. Qin, D. Huang, H. Yi, X. Liu, S. Liu, M. Zhang, B. Li, L. Li, W. Wang, X. Zhou, Y. Li, G. Zeng and C. Lai, *J. Hazard. Mater.* 2022, **422**, 126950.
10. H. Yan, C. Lai, D. Wang, S. Liu, X. Li, X. Zhou, H. Yi, B. Li, M. Zhang, L. Li,

X. Liu, L. Qin and Y. Fu, *J. Mater. Chem. A*, 2021, **9**, 11944-11960.

11. R.-R. Ding, W.-Q. Li, C.-S. He, Y.-R. Wang, X.-C. Liu, G.-N. Zhou and Y. Mu, *Appl. Catal. B: Environ.* 2021, **291**, 120069.

12. X. Wang, X. Zhang, Y. Zhang, Y. Wang, S.-P. Sun, W. D. Wu and Z. Wu, *J. Mater. Chem. A*, 2020, **8**, 15513-15546.

13. D. Ma, H. Yi, C. Lai, X. Liu, X. Huo, Z. An, L. Li, Y. Fu, B. Li, M. Zhang, L. Qin, S. Liu and L. Yang, *Chemosphere*, 2021, **275**, 130104.

14. L. Li, C. Lai, F. Huang, M. Cheng, G. Zeng, D. Huang, B. Li, S. Liu, M. Zhang, L. Qin, M. Li, J. He, Y. Zhang and L. Chen, *Water Res.* 2019, **160**, 238-248.

15. J. Wang, C. Liu, J. Feng, D. Cheng, C. Zhang, Y. Yao, Z. Gu, W. Hu, J. Wan and C. Yu, *J. Hazard. Mater.* 2020, **394**, 122567.

16. Y. Zhong, X. Liang, Z. He, W. Tan, J. Zhu, P. Yuan, R. Zhu and H. He, *Appl. Catal. B: Environ.* 2014, **150-151**, 612-618.

17. J. Wang and J. Tang, *J. Mol. Liq.* 2021, **332**, 115755.

18. M. Munoz, Z. M. de Pedro, J. A. Casas and J. J. Rodriguez, *Appl. Catal. B: Environ.* 2015, **176-177**, 249-265.

19. H. Barndõk, L. Blanco, D. Hermosilla and Á. Blanco, *Chem. Eng. J.* 2016, **284**, 112-121.

20. B. Yang, P. Zhou, X. Cheng, H. Li, X. Huo and Y. Zhang, *J. Colloid Interf. Sci.* 2019, **555**, 383-393.

21. Z. Wang, C. Lai, L. Qin, Y. Fu, J. He, D. Huang, B. Li, M. Zhang, S. Liu, L. Li, W. Zhang, H. Yi, X. Liu and X. Zhou, *Chem. Eng. J.* 2020, **392**, 124851.

22. G. Wang, D. Zhao, F. Kou, Q. Ouyang, J. Chen and Z. Fang, *Chem. Eng. J.* 2018, **351**, 747-755.

23. J. Gao, Y. Liu, X. Xia, L. Wang and W. Dong, *J. Hazard. Mater.* 2018, **353**, 393-400.

24. Z. Zhao, S. Pan, Y. Ye, X. Zhang and B. Pan, *Chem. Eng. J.* 2020, **381**, 122667.

25. H. Wang, M. Jing, Y. Wu, W. Chen and Y. Ran, *J. Hazard. Mater.* 2018, **353**, 53-61.

26. J. Bai, Y. Liu, X. Yin, H. Duan and J. Ma, *Appl. Surf. Sci.* 2017, **416**, 45-50.

27. Y. Liu, H. Cheng, M. Cheng, Z. Liu, D. Huang, G. Zhang, B. Shao, Q. Liang, S. Luo, T. Wu and S. Xiao, *Chem. Eng. J.* 2020, **417**, 127914.

28. L. Lyu, L. Zhang, G. He, H. He and C. Hu, *J. Mater. Chem. A*, 2017, **5**, 7153-7164.

29. X. Hou, X. Huang, F. Jia, Z. Ai, J. Zhao and L. Zhang, *Environ. Sci. Technol.* 2017, **51**, 5118-5126.

30. X. Huang, Y. Chen, E. Walter, M. Zong, Y. Wang, X. Zhang, O. Qafoku, Z. Wang and K. M. Rosso, *Environ. Sci. Technol.* 2019, **53**, 10197-10207.

31. Y. Zhu, R. Zhu, Y. Xi, J. Zhu, G. Zhu and H. He, *Appl. Catal. B: Environ.* 2019, **255**, 117739.

32. X. Wei, H. Yi, C. Lai, X. Huo, D. Ma and C. Du, *J. Colloid Interf. Sci.* 2022, **608**, 942-953.

33. T. Yang, D. Yu, D. Wang, T. Yang, Z. Li, M. Wu, M. Petru and J. Crittenden, *Appl. Catal. B: Environ.* 2021, **286**, 119859.

34. M. Ahmad, X. Quan, S. Chen and H. Yu, *Appl. Catal. B: Environ.* 2020, **264**, 118534.

35. X. Huang, X. Hou, F. Jia, F. Song, J. Zhao and L. Zhang, *ACS Appl. Mater. Inter.* 2017, **9**, 8751-8758.

36. Z. W. Chen, L. X. Chen, C. C. Yang and Q. Jiang, *J. Mater. Chem. A*, 2019, **7**, 3492-3515.

37. X.-F. Yang, A. Wang, B. Qiao, J. Li, J. Liu and T. Zhang, *Accounts Chem. Res.* 2013, **46**, 1740-1748.

38. J. Y. T. Chan, S. Y. Ang, E. Y. Ye, M. Sullivan, J. Zhang and M. Lin, *Phys. Chem. Chem. Phys.* 2015, **17**, 25333-25341.

39. J. Zan, H. Song, S. Zuo, X. Chen, D. Xia and D. Li, *J. Clean. Prod.* 2020, **246**, 118971.

40. H. Jin, X. Tian, Y. Nie, Z. Zhou, C. Yang, Y. Li and L. Lu, *Environ. Sci. Technol.* 2017, **51**, 12699-12706.

41. K. Pan, C. Yang, J. Hu, W. Yang, B. Liu, J. Yang, S. Liang, K. Xiao and H. Hou, *J. Hazard. Mater.* 2020, **389**, 122072.

42. N. Thomas, D. D. Dionysiou and S. C. Pillai, *J. Hazard. Mater.* 2021, **404**, 124082.

43. N. Farhadian, S. Liu, A. Asadi, M. Shahlaei and S. Moradi, *J. Mol. Liq.* 2021, **321**, 114896.

44. J. Wang and J. Tang, *Chemosphere*, 2021, **276**, 130177.

45. S. D. Taylor, L. Kovarik, J. B. Cliff and K. M. Rosso, *Environ. Sci. Nano*, 2019,

6, 2429-2440.

46. Y. Zhao, F. Pan, H. Li, T. Niu, G. Xu and W. Chen, *J. Mater. Chem. A*, 2013, **1**, 7242-7246.

47. M. Qin, B. Lu, S. Feng, Z. Zhen, R. Chen and H. Liu, *Chemosphere*, 2019, **230**, 286-293.

48. S.-S. Lin and M. D. Gurol, *Environ. Sci. Technol.* 1998, **32**, 1417-1423.

49. C. M. Lousada, A. J. Johansson, T. Brinck and M. Jonsson, *J. Phys. Chem. C*, 2012, **116**, 9533-9543.

50. X. Liao, F. Wang, F. Wang, Y. Cai, Y. Yao, B.-T. Teng, Q. Hao and L. Shuxiang, *Appl. Catal. B: Environ.* 2019, **259**, 118064.

51. M. Zong, D. Song, X. Zhang, X. Huang, X. Lu and K. M. Rosso, *Environ. Sci. Technol.* 2021, **55**, 677-688.

52. J. Liu, X. Li, B. Liu, C. Zhao, Z. Kuang, R. Hu, B. Liu, Z. Ao and J. Wang, *ACS Appl. Mater. Inter.* 2018, **10**, 38051-38056.

53. Dai, Chu, Tian, Xike, Nie, Yulun, Lin, Hong-Ming, Yang and Chao, *Environ. Sci. Technol.* 2018, **52**, 6518-6525.

54. G. Liu, H. G. Yang, J. Pan, Y. Q. Yang, G. Q. Lu and H.-M. Cheng, *Chem. Rev.* 2014, **114**, 9559-9612.

55. Y. Zhong, L. Yu, Z.-F. Chen, H. He, F. Ye, G. Cheng and Q. Zhang, *ACS Appl. Mater. Inter.* 2017, **9**, 29203-29212.

56. Y. Chen, C. J. Miller and T. D. Waite, *Environ. Sci. Technol.* 2021, 55, 14414-14425.

57. H. Li, J. Shang, Z. Yang, W. Shen, Z. Ai and L. Zhang, *Environ. Sci. Technol.* 2017, **51**, 5685-5694.

58. Y. Nosaka and A. Nosaka, *ACS Energy Lett.* 2016, **1**, 356-359.

59. J. Luo, D. Yu, K. D. Hristovski, K. Fu, Y. Shen, P. Westerhoff and J. C. Crittenden, *Environ. Sci. Technol.* 2021, **55**, 4287-4304.

60. J. Luo, Y. Liu, C. Fan, L. Tang, S. Yang, M. Liu, M. Wang, C. Feng, X. Ouyang, L. Wang, L. Xu, J. Wang and M. Yan, *ACS Catal.* 2021, **11**, 11440-11450.

61. A. V. Marenich, C. J. Cramer and D. G. Truhlar, *J. Phys. Chem. B*, 2009, **113**, 6378-6396.

62. J. Deng, C. Ye, A. Cai, L. Huai, S. Zhou, F. Deng, X. Li and X. Ma, *Chem. Eng. J.* 2021, **420**, 129863.

63. L. Lyu, L. Zhang and C. Hu, *Environ. Sci. Nano*, 2016, **3**, 1483-1492.

64. S. Guo, H. Wang, W. Yang, H. Fida, L. You and K. Zhou, *Appl. Catal. B: Environ.* 2020, **262**, 118250.

65. Y. Gao, W. Zhu, J. Liu, P. Lin, J. Zhang, T. Huang and K. Liu, *Appl. Catal. B: Environ.* 2021, **295**, 120273.

66. M. K. Panjwani, Q. Wang, Y. Ma, Y. Lin, F. Xiao and S. Yang, *Environ. Sci. Nano*, 2021, **8**, 2204-2213.

67. Q. Ji, L. Bi, J. Zhang, H. Cao and X. S. Zhao, *Energ. Environ. Sci.* 2020, **13**, 1408-1428.

68. K. Zhu, F. Shi, X. Zhu and W. Yang, *Nano Energy*, 2020, **73**, 104761.

69. T. Soltani and B.-K. Lee, *J. Mol. Catal. A: Chem.* 2016, **425**, 199-207.

70. X. X. Guo, T. T. Hu, B. Meng, Y. Sun and Y.-F. Han, *Appl. Catal. B: Environ.* 2020, **260**, 118157.

71. L. Wu, J. Hong, Q. Zhang, B.-Y. Chen, J. Wang and Z. Dong, *Chem. Eng. J.* 2020, **385**, 123620.

72. Y. Bu, H. Li, W. Yu, Y. Pan, L. Li, Y. Wang, L. Pu, J. Ding, G. Gao and B. Pan, *Environ. Sci. Technol.* 2021, **55**, 2110-2120.

73. S. Zhan, H. Zhang, X. Mi, Y. Zhao, C. Hu and L. Lyu, *Environ. Sci. Technol.* 2020, **54**, 8333-8343.

74. Y. Wang, P. Zhang, T. Li, L. Lyu, Y. Gao and C. Hu, *J. Hazard. Mater.* 2021, **408**, 124818.

75. C. Chen, K. Xu, X. Ji, B. Zhang, L. Miao and J. Jiang, *J. Mater. Chem. A*, 2015, **3**, 12461-12467.

76. X. Zhang, X. Liu, Y. Zeng, Y. Tong and X. Lu, *Small Methods*, 2020, **4**, 1900823.

77. W. Wang, Y. Liu, Y. Yue, H. Wang, G. Cheng, C. Gao, C. Chen, Y. Ai, Z. Chen and X. Wang, *ACS Catal.* 2021, **11**, 11256-11265.

78. C. Zhou, L. Zhu, L. Deng, H. Zhang, H. Zeng and Z. Shi, *Sep. Purif. Technol.* 2021, **276**, 119404.

79. H. Kuang, Z. He, M. Li, R. Huang, Y. Zhang, X. Xu, L. Wang, Y. Chen and S. Zhao, *Chem. Eng. J.* 2021, **417**, 127987.

80. W. Liu, J. Tian, C. Mao, Z. Wang, J. Liu, R. A. Dahlgren, L. Zhang and X. Wang, *Anal. Chim. Acta*, 2020, **1127**, 246-255.

81. Y. Shang, X. Xu, B. Gao, S. Wang and X. Duan, *Chem. Soc. Rev.* 2021, **50**,

5281-5322.

82. Y. Chen, S. Ji, C. Chen, Q. Peng, D. Wang and Y. Li, *Joule*, 2018, **2**, 1242-1264.

83. M. Xu, C. Lai, X. Liu, B. Li, M. Zhang, F. Xu, S. Liu, L. Li, L. Qin, H. Yi and Y. Fu, *J. Mater. Chem. A*, 2021, **9**, 24148-24174.

84. W. Yang, P. Hong, D. Yang, Y. Yang, Z. Wu, C. Xie, J. He, K. Zhang, L. Kong and J. Liu, *J. Colloid Interf. Sci.* 2021, **597**, 56-65.

85. M. Zhang, C. Lai, B. Li, S. Liu, D. Huang, F. Xu, X. Liu, L. Qin, Y. Fu, L. Li, H. Yi and L. Chen, *Small*, 2021, **17**, 2007113.

86. Y. J. Chen, S. F. Ji, Y. G. Wang, J. C. Dong, W. X. Chen, Z. Li, R. A. Shen, L. R. Zheng, Z. B. Zhuang, D. S. Wang and Y. D. Li, *Angew. Chem. Int. Edit.* 2017, **56**, 6937-6941.

87. Y. Yin, L. Shi, W. Li, X. Li, H. Wu, Z. Ao, W. Tian, S. Liu, S. Wang and H. Sun, *Environ. Sci. Technol.* 2019, **53**, 11391-11400.

88. Y. Gao, C. Yang, M. Zhou, C. He, S. Cao, Y. Long, S. Li, Y. Lin, P. Zhu and C. Cheng, *Small*, 2020, **16**, 2005060.

89. F. Chen, X.-L. Wu, C. Shi, H. Lin, J. Chen, Y. Shi, S. Wang and X. Duan, *Adv. Funct. Mater.* 2021, **31**, 2007877.

90. A. Wang, J. Li and T. Zhang, *Nat. Rev. Chem.* 2018, **2**, 65-81.

91. L. Su, P. Wang, X. Ma, J. Wang and S. Zhan, *Angew. Chem. Int. Edit.* 2021, **60**, 21261-21266.

92. Y. Gao, X. Duan, B. Li, Q. Jia, Y. Li, X. Fan, F. Zhang, G. Zhang, S. Wang and W. Peng, *J. Mater. Chem. A*, 2021, **9**, 14793-14805.

93. J. Li, L. Zhang, K. Doyle-Davis, R. Li and X. Sun, *Carbon Energy*, 2020, **2**, 488-520.

94. R. Bliem, J. E. S. v. d. Hoeven, J. Hulva, J. Pavelec, O. Gamba, P. E. d. Jongh, M. Schmid, P. Blaha, U. Diebold and G. S. Parkinson, *P. Natl. Acad. Sci.* 2016, **113**, 8921-8926.

95. A. Han, B. Wang, A. Kumar, Y. Qin, J. Jin, X. Wang, C. Yang, B. Dong, Y. Jia, J. Liu and X. Sun, *Small Methods*, 2019, **3**, 1800471.

96. T. Zhu, Y. Han, S. Liu, B. Yuan, Y. Liu and H. Ma, *Front. Chem.* 2021, **9**, 717201.

97. S. Zuo, X. Jin, X. Wang, Y. Lu, Q. Zhu, J. Wang, W. Liu, Y. Du and J. Wang, *Appl. Catal. B: Environ.* 2021, **282**, 119551.

98. X. Chen, D.-D. Ma, B. Chen, K. Zhang, R. Zou, X.-T. Wu and Q.-L. Zhu, *Appl. Catal. B: Environ.* 2020, **267**, 118720.

99. S. Zhang, T. Hedtke, X. Zhou, M. Elimelech and J.-H. Kim, *ACS EST Engg.* 2021, **1**, 706-724.

100. Y. Chen, C. Zhang, H. Liu and J. Qu, *Angew. Chem. Int. Edit.* 2019, **58**, 8134-8138.

101. M. Zhang, C. Xiao, X. Yan, S. Chen, C. Wang, R. Luo, J. Qi, X. Sun, L. Wang and J. Li, *Environ. Sci. Technol.* 2020, **54**, 10289-10300.

102. C. Liu, J. Li, J. Qi, J. Wang, R. Luo, J. Shen, X. Sun, W. Han and L. Wang, *ACS Appl. Mater. Inter.* 2014, **6**, 13167-13173.

103. J. Qian, X. Gao and B. Pan, *Environ. Sci. Technol.* 2020, **54**, 8509-8526.

104. P. Su, W. Fu, X. Du, G. Song, Y. Tang and M. Zhou, *Sep. Purif. Technol.* 2021,

276, 119232.

105. S. Zhang, M. Sun, T. Hedtke, A. Deshmukh, X. Zhou, S. Weon, M. Elimelech and J.-H. Kim, *Environ. Sci. Technol.* 2020, **54**, 10868-10875.

106. S. Zhang, T. Hedtke, Q. Zhu, M. Sun, S. Weon, Y. Zhao, E. Stavitski, M. Elimelech and J.-H. Kim, *Environ. Sci. Technol.* 2021, **55**, 9266-9275.

107. L. Yu, W.-X. Li, X. Pan and X. Bao, *J. Phys. Chem. C*, 2012, **116**, 16461-16466.

108. X. Pan and X. Bao, *Accounts Chem. Res.* 2011, **44**, 553-562.

109. D. Guo, Y. Liu, H. Ji, C.-C. Wang, B. Chen, C. Shen, F. Li, Y. Wang, P. Lu and W. Liu, *Environ. Sci. Technol.* 2021, **55**, 4045-4053.

110. Z. Yang, J. Qian, A. Yu and B. Pan, *P. Natl. Acad. Sci.* 2019, **116**, 6659.

111. B. Wang, L. Xu, G. Liu, Y. Ye, Y. Quan, C. Wang, W. Wei, W. Zhu, C. Xu, H. Li and J. Xia, *J. Alloy. Compd.* 2020, **826**, 154152.

112. J. Li, C. Xiao, K. Wang, Y. Li and G. Zhang, *Environ. Sci. Technol.* 2019, **53**, 11023-11030.

113. L. Yang, H. Yang, S. Yin, X. Wang, M. Xu, G. Lu, Z. Liu and H. Sun, *Small*, 2022, **18**, 2104941.

114. Q. Liu, Y. Liu, H. Li, L. Li, D. Deng, F. Yang and X. Bao, *Appl. Surf. Sci.* 2017, **410**, 111-116.

115. D. Deng, X. Chen, L. Yu, X. Wu, Q. Liu, Y. Liu, H. Yang, H. Tian, Y. Hu, P. Du, R. Si, J. Wang, X. Cui, H. Li, J. Xiao, T. Xu, J. Deng, F. Yang, P. N. Duchesne, P. Zhang, J. Zhou, L. Sun, J. Li, X. Pan and X. Bao, *Sci. Adv.* 2015, **1**, 1500462.

116. X. Li, X. Yang, J. Zhang, Y. Huang and B. Liu, *ACS Catal.* 2019, **9**, 2521-2531.

117. H. Zheng, J. Bao, Y. Huang, L. Xiang, Faheem, B. Ren, J. Du, M. N. Nadagouda and D. D. Dionysiou, *Appl. Catal. B: Environ.* 2019, **259**, 118056.

118. S. Liu, C. Lai, B. Li, X. Liu, X. Zhou, C. Zhang, L. Qin, L. Li, M. Zhang, H. Yi, Y. Fu, H. Yan and L. Chen, *Chem. Eng. J.* 2022, **427**, 131655.

119. S. Rong, P. Zhang, F. Liu and Y. Yang, *ACS Catal.* 2018, **8**, 3435-3446.

120. H. Zhang, C. Li, L. Lyu and C. Hu, *Appl. Catal. B: Environ.* 2020, **270**, 118874.

121. S. An, G. Zhang, T. Wang, W. Zhang, K. Li, C. Song, J. T. Miller, S. Miao, J. Wang and X. Guo, *ACS Nano*, 2018, **12**, 9441-9450.

122. Y. Gao, Y. Zhu, T. Li, Z. Chen, Q. Jiang, Z. Zhao, X. Liang and C. Hu, *Environ. Sci. Technol.* 2021, **55**, 8318-8328.

123. Z. Xiao, Y. Wang, Y.-C. Huang, Z. Wei, C.-L. Dong, J. Ma, S. Shen, Y. Li and S. Wang, *Energy Environ. Sci.* 2017, **10**, 2563-2569.

124. K. Ye, K. Li, Y. Lu, Z. Guo, N. Ni, H. Liu, Y. Huang, H. Ji and P. Wang, *Trend. Anal. Chem.* 2019, **116**, 102-108.

125. X. Li, X. Liu, L. Xu, Y. Wen, J. Ma and Z. Wu, *Appl. Catal. B: Environ.* 2015, **165**, 79-86.

126. A.-H. Lu, J.-J. Nitz, M. Comotti, C. Weidenthaler, K. Schlichte, C. W. Lehmann, O. Terasaki and F. Schüth, *J. Am. Chem. Soc.* 2010, **132**, 14152-14162.

127. Y. Jian, T. Yu, Z. Jiang, Y. Yu, M. Douthwaite, J. Liu, R. Albilali and C. He, *ACS Appl. Mater. Inter.* 2019, **11**, 11369-11383.

128. X. Zhou, Z. Zeng, G. Zeng, C. Lai, R. Xiao, S. Liu, D. Huang, L. Qin, X. Liu, B. Li, H. Yi, Y. Fu, L. Li, M. Zhang and Z. Wang, *Chem. Eng. J.* 2020, **401**,

126127.

129. J. Xiong, J. Di, J. X. Xia, W. S. Zhu and H. M. Li, *Adv. Funct. Mater.*, 2018, **28**, 19.

130. D. Lu, B. Jiang, X. Shen, Z. W. LaTurner, C. Wang, X. Chen, X. Xu and L. Zhu, *Chem. Eng. J.* 2022, **429**, 132164.

131. R. Zhou, S. Liu, F. He, H. Ren and Z. Han, *Chemosphere*, 2021, **285**, 131433.

132. L. Lei, D. Huang, M. Cheng, R. Deng, S. Chen, Y. Chen and W. Wang, *Coordin. Chem. Rev.* 2020, **418**, 213372.

133. A. I. Frenkel, *Chem. Soc. Rev.* 2012, **41**, 8163-8178.

134. Y. Yang, G. Zeng, D. Huang, C. Zhang, D. He, C. Zhou, W. Wang, W. Xiong, B. Song, H. Yi, S. Ye and X. Ren, *Small*, 2020, **16**, 2001634.

135. N. Zhang, X. Li, H. Ye, S. Chen, H. Ju, D. Liu, Y. Lin, W. Ye, C. Wang, Q. Xu, J. Zhu, L. Song, J. Jiang and Y. Xiong, *J. Am. Chem. Soc.* 2016, **138**, 8928-8935.

136. L. Li, S. Liu, M. Cheng, C. Lai, G. Zeng, L. Qin, X. Liu, B. Li, W. Zhang, Y. Yi, M. Zhang, Y. Fu, M. Li and M. Long, *J. Hazard. Mater.* 2021, **406**, 124333.

137. C. Zhou, E. Almatrafi, X. Tang, B. Shao, W. Xia, B. Song, W. Xiong, W. Wang, H. Guo, S. Chen and G. Zeng, *Sep. Purif. Technol.* 2022, **286**, 120464.

138. W. Wang, W. Zhou, W. Li, X. Xiong, Y. Wang, K. Cheng, J. Kang, Q. Zhang and Y. Wang, *Appl. Catal. B: Environ.* 2020, **276**, 119142.

139. L. Zong, X. Chen, S. Dou, K. Fan, Z. Wang, W. Zhang, Y. Du, J. Xu, X. Jia, Q. Zhang, X. Li, Y. Deng, Y. Chen and L. Wang, *Chinese Chemical Letters*, 2020, **32**, 1121-1126.

140. F. Xu, C. Lai, M. Zhang, B. Li, S. Liu, M. Chen, L. Li, Y. Xu, L. Qin, Y. Fu, X. Liu, H. Yi and X. Yang, *J. Colloid Interf. Sci.* 2021, **601**, 196-208.

141. Z.-j. Wang, Y. Xie and C.-j. Liu, *J. Phys. Chem. C*, 2008, **112**, 19818-19824.

142. Y. Liu, J. Zhang, W. Hou and J.-J. Zhu, *Nanotechnology*, 2008, **19**, 135707.

143. T. Zeng, X. Zhang, S. Wang, H. Niu and Y. Cai, *Environ. Sci. Technol.* 2015, **49**, 2350-2357.

144. K. Lee, M. Kim and H. Kim, *J. Mater. Chem.* 2010, **20**, 3791-3789.

145. T. K. Sau and A. L. Rogach, *Adv. Mater.* 2010, **22**, 1781-1804.

146. K. Zhou and Y. Li, *Angew. Chem. Int. Edit.* 2012, **51**, 602-613.

147. Z. Niu and Y. Li, *Chem. Mater.* 2014, **26**, 72-83.

148. C. H. Ho, C. P. Tsai, C. C. Chung, C. Y. Tsai and C. H. Lai, *Chem. Mater.* 2011, **23**, 1753-1760.

149. J. S. Chen, T. Zhu, X. H. Yang, H. G. Yang and X. W. Lou, *J. Am. Chem. Soc.* 2010, **132**, 13162-13164.

150. H. G. Yang, C. H. Sun, S. Z. Qiao, J. Zou, G. Liu, S. C. Smith, H. M. Cheng and G. Q. Lu, *Nature*, 2008, **453**, 638-641.

151. Y. Chen, W. Yang, S. Gao, C. Sun and Q. Li, *ACS Appl. Nano Mater.* 2018, **1**, 3565-3578.

152. J. Shi, Y. Chang, Y. Tang, X. Wang, X. Wang, X. Zhang and J. Cao, *Ceram. Int.* 2020, **46**, 5315-5322.

153. Y. Ling, G. Wang, J. Reddy, C. Wang, J. Z. Zhang and Y. Li, *Angew. Chem. Int. Enit.* 2012, **51**, 4074-4079.

154. S. Xiong, X. Lin, S. Liu, S. Weng, S. Jiang, Y. Jiao, Y. Xu and J. Cheng, *Vacuum*, 2020, **182**, 109692.

155. S. She, J. Yu, W. Tang, Y. Zhu, Y. Chen, J. Sunarso, W. Zhou and Z. Shao, *ACS Appl. Mater. Inter.* 2018, **10**, 11715-11721.

156. Y. Zhao, H. An, G. Dong, J. Feng, T. Wei, Y. Ren and J. Ma, *Chem. Eng. J.* 2020, **388**, 124371.

157. W. Xie, F. Zhou, X. Bi, D. Chen, Z. Huang, Y. Li, S. Sun and J. Liu, *Chemosphere*, 2019, **221**, 563-572.

158. S. Zhao, D. Kang, Y. Liu, Y. Wen, X. Xie, H. Yi and X. Tang, *ACS Catal.* 2020, **10**, 11739-11750.

159. N. Tian, X. Tian, Y. Nie, C. Yang, Z. Zhou and Y. Li, *Chem. Eng. J.* 2019, **355**, 448-456.

160. F. Liu, W. Jin, Y. Li, L. Zheng, Y. Hu, X. Xu, Y. Xue, C. Tang, H. Liu and J. Zhang, *Appl. Surf. Sci.* 2020, **529**, 147125.

161. K.-L. Yan, X. Shang, Z.-Z. Liu, B. Dong, S.-S. Lu, J.-Q. Chi, W.-K. Gao, Y.-M. Chai and C.-G. Liu, *Int. J. Hydrogen Energ.* 2017, **42**, 24150-24158.

162. W. Liu, J. Liu, P. Zhou, R. A. Dahlgren and X. Wang, *J. Colloid Interf. Sci.* 2022, **606**, 688-695.

163. X. Wei, X. Xie, Y. Wang and S. Yang, *J. Environ. Eng.* 2020, **146**, 04020005.

164. J.-Y. Park, Y.-J. Lee, P. K. Khanna, K.-W. Jun, J. W. Bae and Y. H. Kim, *J. Mol. Catal. A: Chem.* 2010, **323**, 84-90.

165. H.-J. Qiu, Y. Ito, W. Cong, Y. Tan, P. Liu, A. Hirata, T. Fujita, Z. Tang and M.

Chen, *Angew. Chem. Int. Edit.* 2015, **54**, 14031-14035.

166. Y. J. Sa, D.-J. Seo, J. Woo, J. T. Lim, J. Y. Cheon, S. Y. Yang, J. M. Lee, D. Kang, T. J. Shin, H. S. Shin, H. Y. Jeong, C. S. Kim, M. G. Kim, T.-Y. Kim and S. H. Joo, *J. Am. Chem. Soc.* 2016, **138**, 15046-15056.

167. H. Wei, K. Huang, D. Wang, R. Zhang, B. Ge, J. Ma, B. Wen, S. Zhang, Q. Li, M. Lei, C. Zhang, J. Irawan, L.-M. Liu and H. Wu, *Nat. Commun.* 2017, **8**, 1490.

168. L. Peng, X. Duan, Y. Shang, B. Gao and X. Xu, *Appl. Catal. B: Environ.* 2021, **287**, 119963.

169. Y. Lei, F. Yang, H. Xie, Y. Lei, X. Liu, Y. Si and H. Wang, *J. Mater. Chem. A*, 2020, **8**, 20629-20636.

170. X. Wang, J. Du, Q. Zhang, L. Gu, L. Cao and H.-P. Liang, *Carbon*, 2020, **157**, 614-621.

171. P. Su, M. Zhou, G. Ren, X. Lu, X. Du and G. Song, *J. Mater. Chem. A*, 2019, **7**, 24408-24419.

172. J. Wang, C. Liu, L. Qi, J. Li, X. Sun, J. Shen, W. Han and L. Wang, *Environ. Pollut.* 2018, **243**, 1068-1077.

173. D. Du, W. Shi, L. Wang and J. Zhang, *Appl. Catal. B: Environ.* 2017, **200**, 484-492.

174. W. Lee and S.-J. Park, *Chem. Rev.* 2014, **114**, 7487-7556.

175. P. Wang, X. Liu, W. Qiu, F. Wang, H. Jiang, M. Chen, W. Zhang and J. Ma, *Water Res.* 2020, **182**, 116030.

176. C. Gao, F. Lyu and Y. Yin, *Chem. Rev.* 2021, **121**, 834-881.

177. S. Valange, R. Palacio, A. Charmot, J. Barrault, A. Louati and Z. Gabelica, *J. Mol. Catal. A: Chem.* 2009, **305**, 24-33.

178. A. Li, W. Zhu, C. Li, T. Wang and J. Gong, *Chem. Soc. Rev.* 2019, **48**, 1874-1907.

179. W. Wang, M. Ding, L. Ma, X. Yang, J. Li, N. Tsubaki, G. Yang, T. Wang and X. Li, *Fuel*, 2016, **164**, 347-351.